

Leptophilic Dark Matter in Single and Multicomponent Frameworks at Future Lepton Colliders

Project-II (PH518) Report

Master of Science

by

Bhavya Ashok Thacker
(222121015)

under the guidance of

Dr. Subhaditya Bhattacharya
Associate Professor



DEPARTMENT OF PHYSICS
INDIAN INSTITUTE OF TECHNOLOGY GUWAHATI
GUWAHATI - 781039, ASSAM

Abstract

Multiple observations in cosmology and astrophysics indicate the existence of a non-luminous matter that dominates our Universe. This non-luminous matter is called Dark Matter and is one of the greatest problems in the history of physics. Collider experiments prove to be an essential direction in the quest for Dark Matter search as well as to constrain New Physics parameters involved in BSM models. The main aim of this project is to study leptophilic Dark Matter scenarios in a model-independent way at the proposed linear electron-positron collider. We use higher dimensional effective operators describing DM-SM interactions. We have investigated two such DM scenarios in this direction, one involving a single component WIMP-like fermionic DM connected to the SM leptons, and another scenario with two DM components, one being scalar and the other being fermionic in nature. In both cases, we studied collider reach in the mono-X detection channel at high energy frontiers. Where X represents SM γ , Z or H.

Certificate

This is to certify that the work contained in the project report titled “*Leptophilic Dark Matter in Single and Multicomponent Frameworks at Future Lepton Colliders*” by Bhavya Ashok Thacker, has been carried out under my supervision at the Department of Physics, and this work has not been submitted elsewhere.

Project Supervisor

Name: Dr. Subhaditya Bhattacharya

Department: Physics

Date: 20th April, 2024

Declaration

This is to declare that the project report titled "*Leptophilic Dark Matter in Single and Multicomponent Frameworks at Future Lepton Colliders*", submitted by me to the Department of Physics, IIT, Guwahati, for the partial fulfillment of the requirement for the coursework for the degree of Master of Science, is a bonafide work carried out by me under the supervision of *Dr. Subhaditya Bhattacharya*. I declare that this report is based on my study and research and I have acknowledged all materials and resources used in its preparation.

Name: Bhavya Ashok Thacker
Roll Number: 222121015
Department: Physics
Date: 20th April, 2024

Acknowledgement

I am profoundly thankful for the exceptional guidance and support provided by my supervisor, Dr. Subhaditya Bhattacharya. His mentorship has been invaluable, constantly directing me on the right path and meticulously reviewing my reports to offer constructive feedback. Once again, I extend my heartfelt gratitude to Dr. Subhaditya Bhattacharya for his continuous support and guidance throughout this project.

I want to express my sincere gratitude to Abhik Sarkar, Dipankar Pradhan, Niloy Mondal, and Sahabub Jahedi for their guidance and continuous support. Their mentorship has played a crucial role in shaping this thesis, providing invaluable lessons and unwavering motivation during challenging times.

I would like to express special gratitude to Abhik Sarkar for his invaluable discussion sessions and for generously sharing his knowledge, particularly in the field of collider phenomenology. His guidance and teaching in this area have greatly contributed to my understanding and learning experience.

Finally, I am immensely grateful to my parents and my little sister for their unwavering support and their constant motivation.

Contents

Abstract	i
Certificate	ii
Declaration	iii
Acknowledgement	iv
1 The Standard Model of Particle Physics	2
1.1 Introduction	2
1.2 The Standard Model Lagrangian	3
1.2.1 The Gauge Term	3
1.2.2 The Fermion Term	4
1.2.3 The Scalar Sector	4
1.2.4 The Yukawa Term	5
2 Dark Matter and where to find it?	7
2.1 Evidences of Dark Matter	7
2.1.1 Rotation curves	7
2.1.2 Gravitational Lensing	8
2.2 The WIMP Miracle: Freeze-Out mechanism	10
2.3 Search strategies for Dark Matter	12
3 Effective Field Theory	15
3.1 Introduction	15
3.2 Fermi's Theory of Weak Interaction: An EFT example	17
3.3 DM-SM Effective Field Theory	19
4 Effective Leptophilic WIMPs	20
4.1 Introduction	20
4.2 DM-SM Effective Operators	21
4.3 DM Constraints	22
4.3.1 Relic Density	23
4.4 Collider search	25
4.4.1 DM production cross section	26
4.4.2 Event Distributions	29
4.4.3 Summary and Conclusion	30

5	Mono-X signal and Two Component DM	32
5.1	Introduction	32
5.2	DM effective Operatos	33
5.3	Collider Analysis	35
5.3.1	\cancel{E} of Individual Operators	35
5.3.2	Signal and Background	36
5.3.3	Signal significance	38
5.4	Summary and Conclusion	41
6	Future Prospects	42
6.1	Revisiting Two component DM framework	42
6.2	Relic Constriant	42
6.3	Conclusion	44
7	Appendix	46
7.1	The Boltzmann Equation	46
7.2	The WIMP case	51
7.3	Introduction to Collider Physics	55
7.3.1	Overview	55
7.3.2	Collider Kinematics	56
7.3.3	Observables	58
7.3.4	Simulation framework	60
	References	67

Chapter 1

The Standard Model of Particle Physics

1.1 Introduction

The Standard Model of particle physics describes the particles and their underlying interactions. It delicately explains how the ideas of local gauge invariance and Lorentz invariance give rise to interactions between quantum fields mediated by gauge bosons. The SM encapsulates spin 1/2 fermions and spin 0 and spin 1 bosons. The fermion sector is divided into quarks and leptons. The fermionic part forms matter whereas the bosons are force carriers responsible for interactions among the particles.

The quarks and leptons are further divided into two subgroups each with three families or generations as described in Table 1.1. Each fermion has an antiparticle with the same mass but an opposite sign quantum number. All charged fermions take part in electromagnetic interactions, described by Quantum Electrodynamics (QED), which is mediated by Photons (γ). The quarks hold a quantum number called color charge and therefore interact with the strong force described by Quantum Chromodynamics (QCD), which is mediated by 8 gluons (g), which also carry color charge. [1]

Table 1.1 [2] outlines the chirality of particles, distinguishing between left-handed (L) and right-handed (R) eigenstates. Neutrinos are solely left-handed, however, charged fermions have been seen in both chirality states. All left-handed fermion participates in the weak interaction, mediated by the charged W^\pm and the neutral Z boson. The electroweak theory, also known as the Glashow-Salam-Weinberg model, unifies the weak force and the electromagnetic force. The Higgs mechanism generates masses of the majority of the particle content within the Standard Model. Table 1.2 gives an overview of the bosons in the SM. The complete gauge structure of the Standard Model is denoted by the group composition,

$$SU(3)_C \times SU(2)_L \times U(1)_Y \longrightarrow SU(3)_C \times U(1)_{EM} \quad (1.1)$$

The $SU(3)_C$ symmetry characterizes QCD, the theory governing the strong interaction among quarks and gluons. The electroweak (EW) theory provides a unified framework of both QED and weak interaction. This theory is structured under the gauge symmetry $SU(2)_L \times U(1)_Y$. Spontaneous symmetry breaking (SSB) within the electroweak sector, leads to the emergence of a gauge group denoted as $SU(3)_C \times U(1)_{EM}$. Here, the indices C, L, and Y denote the color,

left-handed chirality, and hypercharge, respectively [2].

Fermions	Generation			Quantum Numbers			
	1	2	3	Q	I^3	Y	Colour
Leptons	$\begin{pmatrix} \nu_e \\ e \end{pmatrix}_L$	$\begin{pmatrix} \nu_\mu \\ \mu \end{pmatrix}_L$	$\begin{pmatrix} \nu_\tau \\ \tau \end{pmatrix}_L$	0 -1	+1/2 -1/2	-1 -1	-
	e_R	μ_R	τ_R	-1	0	-2	
Quarks	$\begin{pmatrix} u \\ d \end{pmatrix}_L$	$\begin{pmatrix} c \\ s \end{pmatrix}_L$	$\begin{pmatrix} t \\ b \end{pmatrix}_L$	+2/3 -1/3	+1/2 -1/2	+1/3 +1/3	r, g, b
	u_R	c_R	t_R	+2/3	0	4/3	
	d_R	s_R	b_R	-1/3	0	-2/3	

Table 1.1 The Standard Model fermions characterized by their quantum numbers, which include their electric charge (Q), measured in units of the elementary charge (e), the third component of weak isospin (I^3), hypercharge (Y), and color charge (r, g, b , corresponding to red, green, and blue) [2]

Higgs boson (spin = 0)		Mass (GeV)	charge
		125.09	0
Gauge bosons (spin = 1)		Interaction	
photon (γ)	Electromagnetic	0	0
W^\pm	Weak	80.39	± 1
Z	Weak	91.19	0
gluons (g)	Strong	0	0

Table 1.2 An overview of the bosons in the SM.

1.2 The Standard Model Lagrangian

The complete Lagrangian density of the Standard Model can be represented as the combination of four terms outlined as follows:[1]:

$$\mathcal{L}_{\text{SM}} = \mathcal{L}_{\text{Gauge}} + \mathcal{L}_{\text{Dirac}} + \mathcal{L}_{\text{Higgs}} + \mathcal{L}_{\text{Yukawa}} \quad (1.2)$$

1.2.1 The Gauge Term

The Gauge fields are spin 1 bosons. There are 8 Gluons $G_\mu^a (a = 1, \dots, 8)$, three electroweak fields $W_\mu^i (i = 1, 2, 3)$ and one hypercharge field B_μ transforming under the adjoint representation of $SU(3)_C$, $SU(2)_L$ and $U(1)_Y$ respectively. The $\mathcal{L}_{\text{Gauge}}$ describes the kinetic term of the Gauge fields and is written as:

$$\mathcal{L}_{\text{Gauge}} = -\frac{1}{4}B_{\mu\nu}B^{\mu\nu} - \frac{1}{4}W_{\mu\nu}^i W^{i\mu\nu} - \frac{1}{4}G_{\mu\nu}^a G^{a\mu\nu} \quad (1.3)$$

Where the field strength tensors are defined as,

$$B_{\mu\nu} = \partial_\mu B_\nu - \partial_\nu B_\mu, \quad (1.4)$$

$$W_{\mu\nu}^i = \partial_\mu W_\nu^i - \partial_\nu W_\mu^i + g\epsilon^{ijk}W_\mu^jW_\nu^k, \quad (1.5)$$

$$G_{\mu\nu}^a = \partial_\mu G_\nu^a - \partial_\nu G_\mu^a + g_s f^{abc}G_\mu^bG_\nu^c, \quad (1.6)$$

Where ϵ^{ijk} and f^{abc} are the structure constants of the non abelian $SU(2)_L$ and $SU(3)_C$ groups respectively. g_s and g denote the strong and electroweak gauge couplings.

1.2.2 The Fermion Term

As shown in table 1.1, the fermionic part of the SM contains $SU(2)_L$ singlets (right handed fields: l_R^a and q_R^a) and $SU(2)_L$ doublets (left handed fields):

$$l_L^a = \begin{pmatrix} \nu_a \\ l_a \end{pmatrix}_L, \quad q_L^a = \begin{pmatrix} u_a \\ d_a \end{pmatrix}_L \quad (1.7)$$

Where, $a = (1, 2, 3)$ denotes the generation of fermions as shown in 1.1. The term $\mathcal{L}_{\text{Dirac}}$ in the SM lagrangian (1.2) describes the kinetic and gauge boson interaction of the fermions.

$$\mathcal{L}_{\text{Dirac}} = \sum_a i\bar{q}_L^a \not{D} q_L^a + \sum_a i\bar{l}_L^a \not{D} l_L^a + \sum_a i\bar{q}_R^a \not{D} q_R^a + \sum_a i\bar{l}_R^a \not{D} l_R^a, \quad (1.8)$$

Where l_L and l_R are SM leptons, q_L and q_R are SM quarks. And $\not{D} \equiv D_\mu \gamma^\mu$, where D_μ is the covariant derivative defined as,

$$D_\mu = \partial_\mu - ig' Y B_\mu - ig \frac{\tau^i}{2} W_\mu^i - ig_s \frac{\lambda^a}{2} G_\mu^a \quad (1.9)$$

Where, g' (Y), g (τ^i) and g_s (λ^a) denote the coupling strength (generators) of the gauge groups $U(1)_Y$, $SU(2)_L$ and $SU(3)_C$ respectively. The generators of $SU(3)_C$, denoted as λ^a , can be expressed as 3×3 matrices and are known as the Gell-Mann matrices. The generators of $SU(2)_L$ are given by, $\tau^i = \frac{\sigma^i}{2}$, where σ^i are Pauli matrices, [3]

$$\sigma^1 = \begin{pmatrix} 0 & 1 \\ 1 & 0 \end{pmatrix}, \quad \sigma^2 = \begin{pmatrix} 0 & -i \\ i & 0 \end{pmatrix}, \quad \sigma^3 = \begin{pmatrix} 1 & 0 \\ 0 & -1 \end{pmatrix} \quad (1.10)$$

1.2.3 The Scalar Sector

As seen in section 2.2.1, the gauge lagrangian does not allow a mass term of the gauge bosons as such a term would not be gauge invariant. However, from the table 1.2 it is clear that the gauge bosons (W^\pm, Z) involved in weak interactions are massive. This can be achieved by introducing a complex scalar $SU(2)$ doublet, the Higgs field, Φ , with four degrees of freedom.

$$\Phi = \frac{1}{\sqrt{2}} \begin{pmatrix} \phi_1 + i\phi_2 \\ \phi_3 + i\phi_4 \end{pmatrix} \quad (1.11)$$

The dynamics of the Higgs field is given by the scalar Lagrangian term,

$$L_{\text{scalar}} = (D_\mu \Phi)^\dagger (D_\mu \Phi) - V(\Phi) \quad (1.12)$$

Where the D_μ is the covariant derivative defined as,

$$D_\mu = \partial_\mu - ig' Y B_\mu - ig \frac{\tau^i}{2} W_\mu^i \quad (1.13)$$

$$V(\Phi) = -\mu^2 |\Phi|^2 + \lambda |\Phi|^4 \quad (1.14)$$

The parameters g and g' represent the gauge couplings associated with the $U(1)$ and $SU(2)_L$ groups, respectively. $V(\Phi)$ refers to the well-known Mexican Hat potential characterized by μ and λ , where μ has dimensions of 1 and λ is dimensionless. The minimum point of the Higgs potential $V(\Phi)$ resides on a circle determined by $\sqrt{\frac{\mu^2}{\lambda}}$, known as the Vacuum Expectation Value (VEV) denoted as v .

The symmetry of the ground state is broken when a particular value of phase is selected,

$$\Phi = \frac{1}{\sqrt{2}} \begin{pmatrix} 0 \\ v + h \end{pmatrix} \quad (1.15)$$

When substituting equation (1.2.3) into the scalar Lagrangian alongside the definition of the covariant derivative, the mass terms for three gauge fields are reformulated as follows, [3] [2]

$$\begin{pmatrix} Z_\mu \\ A_\mu \end{pmatrix} = \begin{pmatrix} \cos \theta_W & -\sin \theta_W \\ \sin \theta_W & \cos \theta_W \end{pmatrix} \begin{pmatrix} W_\mu^3 \\ B_\mu \end{pmatrix} \quad (1.16)$$

And,

$$W_\mu^\pm = \frac{W_\mu^1 \mp i W_\mu^2}{\sqrt{2}} \quad (1.17)$$

Here, θ_W is called the Weinberg angle and is defined as follows,

$$\tan \theta_W = \frac{g'}{g} \quad (1.18)$$

After SSB the Higgs boson acquires a mass in terms of vev, v and Higgs Self Coupling, λ . The masses of W^\pm and Z boson can be written in terms of vev, v and the Weinberg angle, θ_W ,

$$\begin{aligned} M_h &= \sqrt{2\lambda}v & M_W &= \frac{gv}{2} \\ M_Z &= \frac{gv}{2 \cos \theta_W} & M_A &= 0 \end{aligned}$$

1.2.4 The Yukawa Term

The Fermion Lagrangian describes the kinetic term of Quarks and Leptons and their gauge interactions. The mass term of the fermions can be generated by introducing the Higgs doublet and writing the Yukawa term as follows:

$$\mathcal{L}_{\text{Yukawa}} = -(y^l)_{ij} \bar{L}_i \Phi l_{Rj} - (y^u)_{ij} \bar{Q}_i \tilde{\Phi} u_{Rj} - (y^d)_{ij} \bar{Q}_i \Phi d_{Rj} + \text{h.c.} \quad (1.19)$$

After the electroweak SSB, the Yukawa Lagrangian can be written as,

$$\mathcal{L}_{\text{Yukawa}} = \left(\frac{v+h}{\sqrt{2}}\right) [-(y^l)_{ij} \bar{l}_i l_{Rj} - (y^u)_{ij} \bar{u}_{Ri} u_{Lj} - (y^d)_{ij} \bar{d}_{Li} d_{Rj} + \text{h.c.}] \quad (1.20)$$

Where the conjugate $\tilde{\Phi}$ is introduced to generate mass terms of up type quarks and it is defined as, $\tilde{\Phi} \equiv i\sigma\Phi^*$. The terms, y^l, y^u, y^d are 3×3 complex matrices in the flavor basis.

Chapter 2

Dark Matter and where to find it?

The Standard Model of Particle Physics and General Relativity stand as two of the most successful frameworks in the history of Physics. With the discovery of the Higgs Boson at the Large Hadron Collider in 2012 and defending a multitude of experimental tests over the past decades, the Standard Model of particle physics remains an incredibly precise framework for understanding phenomena at the smallest scales. On the other extreme, the perihelion precession of Mercury's orbit, Gravitational lensing and the detection of Gravitational Waves by LIGO and VIRGO collaboration in 2015 confirms General Relativity as an accurate description at larger scales. However, despite its success, the Standard Model appears to be incomplete. Cosmological observations concerning the matter-energy density of the universe have revealed that approximately 70% of the universe's energy density is attributed to a cosmological constant factor within Einstein's equations, known as Dark Energy. The remaining 30% comprises non-relativistic matter, with only 5% being ordinary baryonic matter, observable and constituting us. Around 25% budget of the universe comprises of an invisible component called *Dark Matter*.

2.1 Evidences of Dark Matter

The Dark Matter problem is essentially a missing mass problem that has puzzled physicists for many decades. Our story starts in 1884 when Lord Kelvin, pioneered concrete ideas of applying the kinetic theory of gases to stellar systems. Impressed by his notion, Henry Poincaré applied the theory to estimate the mass content in the Milky Way that could reproduce the measured orbital velocity of the Sun. His groundbreaking work laid the foundation for Jacobus Kapteyn and Jan Oort, who investigated stellar kinematics to measure the overall matter density near the Sun. Their findings suggested the existence of a significant amount of "missing mass" (Dark Matter) to explain stellar dynamics accurately. [4] [3]

2.1.1 Rotation curves

In the 1930s, a Swiss Astronomer, Fritz Zwicky studied the orbital velocity of galaxies in the Coma cluster located about 300 million light years from the Earth. He found out that the mass of the visible galaxies is way smaller than their fast orbital motion. He concluded that there must be

some invisible mass or Dark Matter halo to explain the large orbital velocity of the galaxies. [3]

The classic evidence of the missing mass problem came from the studies of rotation curves of galaxies in 1970's by Vera Rubin. For a spherical matter distribution, using Newtonian dynamics we can find out the radial velocity of stars from the center of the galaxy as,

$$v(r) = \sqrt{\frac{GM(r)}{r}} \quad (2.1)$$

$$M(r) = \int_0^r \rho(r') d^3r'$$

Where $M(r)$ is the mass enclosed in a sphere of radius, r and G , is the gravitational constant. Now for very large distances that extend beyond the galactic disc ($r \gg R_{disc}$), M remains constant assuming it to be concentrated in the sphere of radius R . Therefore at large distances, [5]

$$v(r) = \sqrt{\frac{GM(R)}{r}} \approx \frac{1}{\sqrt{r}} \quad (2.2)$$

However, observations of galaxy rotation curves revealed a flattening at greater distances. This discrepancy must be addressed by introducing another invisible component known as a Dark Matter halo, which possesses an increasing mass distribution extending into the outer regions of galaxies.

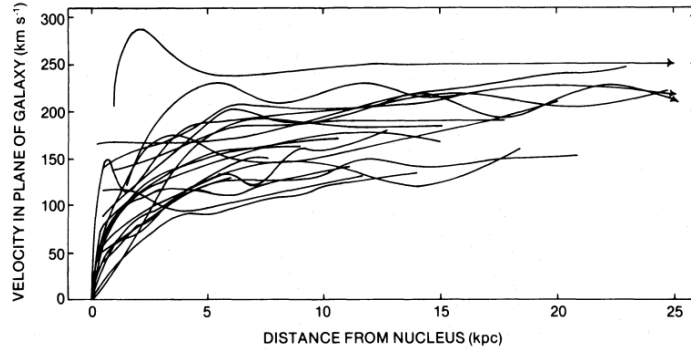


Fig. 2.1 Rotation curves of spiral galaxies showing the flattening behavior at larger distances. [5] The image is taken from a paper by Rubin 1980 [6]

2.1.2 Gravitational Lensing

General Relativity predicts that in the presence of a massive object, light can be deviated by its gravitational potential and therefore does not propagate in a straight line as one would expect for a flat space-time curvature. One can calculate the deflection angle $\delta\phi$ of a light ray as it passes near an object of mass m , [3]

$$\delta\phi = \frac{4G_N m}{a} \quad (2.3)$$

The parameter "a" denotes the impact parameter of the incident photon. Hence, by measuring the deflection angle of incoming photons, one can deduce the mass of a massive object, M , positioned between a source of photons and an observer.

In scenarios where an extremely dense region exists between a source and an observer, light emitted from the source may follow multiple geodesics to reach the observer. This phenomenon leads to the appearance of multiple images of the same physical source. This is called Strong Lensing and has been widely used to measure the masses of galaxies. In the Weak Lensing regime, the apparent shape of luminous objects is distorted by the gravitational potential of massive structures (Like clusters) situated near the line of sight between the source and the observer. While galaxies typically exhibit a circular average shape, the shearing, the shearing effect caused by weak lensing, results in an average ellipsoidal shape. This allows us to measure gravitational potential along a given line of sight, which in turn can measure the total mass of the massive structures.



Fig. 2.2 (a) Einstein ring/arcs due to *SDSSJ0146 – 0929* galaxy cluster as a result of Strong Lensing; Credits: NASA/Hubble Space Telescope [7]. (b) Bullet Cluster (1E0657-56) Credits: NASA/ESA [8]

One of the most convincing indications of Dark Matter’s existence stems from the weak lensing mass contours observed within the Bullet cluster. This cluster comprises of two merging clusters, as illustrated in Figure 2.2. Weak lensing can be utilized to infer the total mass distribution, while the distribution of luminous mass was determined through X-ray emission from the hot intra-cluster gas. In Figure 2.2 b, the blue region represents the mass distribution from weak lensing, while the pink region depicts the X-ray emissions from hot gas. Clearly, the gases of the two clusters interacted as they passed through each other. However, the total mass distributions of the clusters coincide with the positions of the galaxies, showing spherical shapes. This suggests that most of the mass components in the colliding clusters did not interact, thus demonstrating the collisionless nature of Dark Matter. Such an observation provides compelling support for the particle interpretation of Dark Matter, in contrast to modified gravity theories. [3]

Following these strong pieces of evidence, it is natural to ask questions about the origin of the observed Dark Matter. One way to answer this is to incorporate a new Dark Matter particle which is to look Beyond the Standard Model (BSM) and find out its relic abundance¹. From the experiments, it is clear that this particle interacts weakly with the Standard Model particles.

¹DM relic abundance: Measured by Planck satellite from observation of CMB data in the Λ CDM model of cosmology

Therefore, in the 1980s *Weakly Interacting Massive Particle* (WIMP) as a Dark Matter model was introduced. WIMP as its name suggests interacts weakly with Standard Model particles. WIMP was assumed to be in thermal equilibrium with SM particles, that decoupled at some early stage of the Universe. The calculations of which have been done in the following section. This idea still remains the most popular solution to explain the Dark Matter relic density.

2.2 The WIMP Miracle: Freeze-Out mechanism

Particles in the early universe were in thermal and chemical equilibrium with each other. However, as the universe expanded departures from thermal equilibrium led to Dark Matter relic, a constant baryon number density, and so on.

The idea behind a particle species to be either coupled or decoupled depends on the interaction rate, Γ , and the expansion rate of the universe, H : [9]

$$\Gamma \leq H(\text{Decoupled}) \quad (2.4)$$

$$\Gamma \geq H(\text{Coupled}) \quad (2.5)$$

The Freeze-Out condition refers to the former idea i.e. when $\Gamma \leq H$. Dark Matter - Standard Model interactions stopped and it lead to constant Dark Matter relic density. Recalling the Boltzmann equation we derived for the WIMP case (see Appendix: WIMP) and also keeping in mind that the Boltzmann equation is a first-order non-linear differential equation, for which no general analytical solutions are possible. Thus, we need to rely on numerical solutions. [9] [10]

$$\frac{dY}{dt} = -\frac{\lambda}{x^{n+2}}[Y^2 - (Y^{eq})^2] \quad (2.6)$$

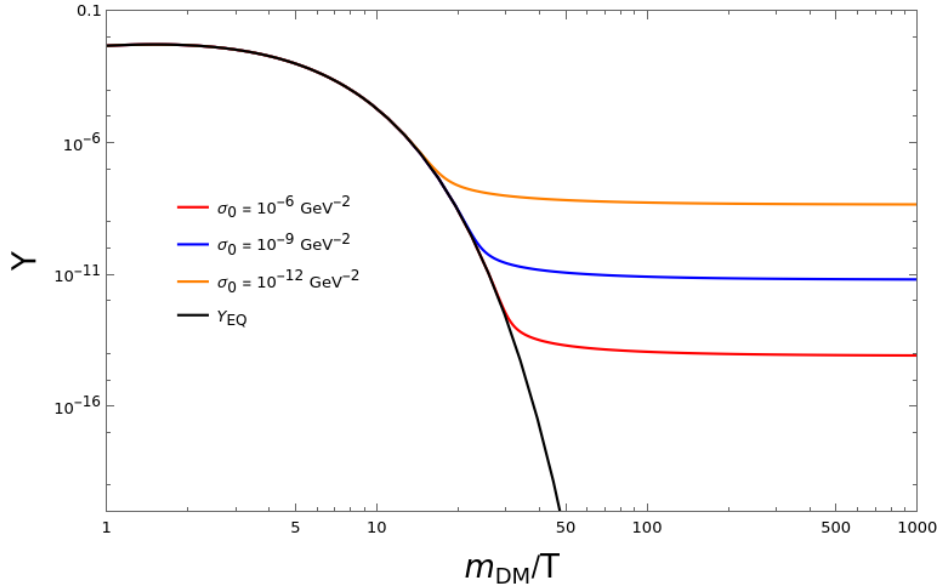


Fig. 2.3 The logarithmic plot illustrates the decoupling of a cold Dark Matter relic with a mass of $m_{\text{DM}} = 100 \text{ GeV}$ and $n = 0$. The black line represents the equilibrium distribution, while the other lines depict the actual abundance.

As depicted in Figure 2.3, the WIMP freezes out shortly after decoupling from equilibrium (represented by the black line) with the thermal bath. Here, σ_0 denotes the interaction cross-section, which is incorporated into λ . The plot clearly shows that a stronger interaction (i.e., a larger cross-section, σ_0) results in a later freeze-out, thereby yielding a lower relic density.

For a cold relic, after freeze out the number density is much larger than the equilibrium number density (exponentially decay factor) as seen in the plot. Therefore, we can write, [11]

$$\frac{dY}{dt} \approx -\frac{\lambda}{x^{n+2}} Y^2 \quad (2.7)$$

Integrating this differential equation with limits from $x = x_f$ to $x = \infty$. Where x_f is the lower limit at which this approximation holds.

$$Y_\infty \approx Y_{\text{today}} \approx \frac{n+1}{\lambda} x_f^{n+1} \quad (2.8)$$

The quantity $Y_{\text{today}} \approx Y_\infty$ is what we plug into Ωh^2 to check if we have obtained the correct observed dark matter relic density. [11]

Relic Density

The relic density is the mass density of the species in terms of the critical density in a co-moving volume. It is given as,

$$\Omega h^2 = \frac{\rho}{\rho_c} h^2 \quad (2.9)$$

Where,

Ω represents the cosmological density, while h denotes the reduced Hubble constant.

ρ = Present energy density of the species = $m_{DM} n = m_{DM} s_0 Y_\infty$

n = number density of the species

s_0 = entropy density of the universe at present = $7.04 n_\gamma$

n_γ = number density of photons at present $\approx 405 \text{ cm}^{-3}$

Y_∞ = Yield at present = Yield at the freeze-out

$h = 0.01 \frac{H_0}{\text{km/s/Mpc}} = 0.01 * 69.8 = 0.698$

ρ_c = critical density = $\frac{3H_0^2}{8\pi G} = 5.05 \text{ GeV}/m^3$

Putting all the values in equation (2.43), we get,

$$\Omega h^2 = 2.751 \times 10^8 \frac{m_{DM}}{\text{GeV}} Y_\infty \quad (2.10)$$

Where the observed relic density data taken from the current Planck data is [12],

$$\Omega h^2 = 0.11933 \pm 0.00091 \quad (2.11)$$

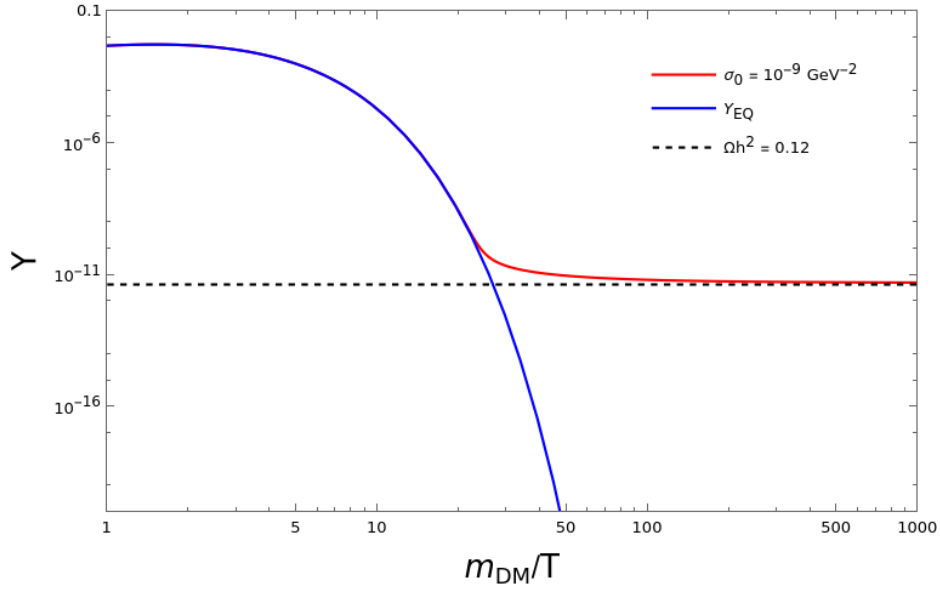


Fig. 2.4 Here, the black dotted line shows yield at infinity which gives the correct relic density and corresponds to $\sigma_0 = 1.33 \times 10^{-9}$ for $m_{DM} = 100$ GeV and $n = 0$

Here, the Dark Matter mass taken to be 100 GeV is roughly in the ballpark of an electroweak mass scale, and the fact that the annihilation cross section of roughly 10^{-9}GeV^{-2} which is a typical electroweak cross-section gave the correct Dark Matter relic density is known as the *WIMP miracle*.

2.3 Search strategies for Dark Matter

We discussed WIMP as a Dark Matter particle in Beyond the Standard Model construction. Recalling that WIMP interacts weakly with Standard Model particles. Under the assumption that such a coupling does exist, the potential methods for detecting Dark Matter can be divided into three categories. [3]

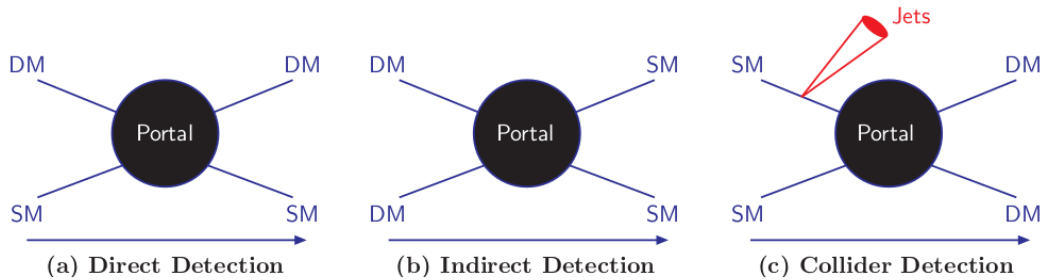


Fig. 2.5 Pictorial representation of Dark Matter searches. The image is taken from [3]

I. Direct Detection

Direct detection refers to the following process,

$$DM + SM \rightarrow DM + SM$$

The basic strategy behind this method is to measure the the recoil energy of a nucleus as it scatters off a Dark Matter particle. However, the expected occurrence of events for this process is notably small. Therefore, most of the experiments aimed at direct detection are located deep underground to avoid any background contamination. Detectors measure nuclear recoils using mainly three techniques, primarily based on measuring ionization, phonons, or scintillation. The current ongoing experiments include, XENON1T, PICASSO, LUX, etc

II. Indirect Detection

Indirect detection refers to the following process,

$$DM + DM \rightarrow SM + SM$$

Where DM annihilation to the SM particles could produce, leptons ($\uparrow\downarrow$), quarks (q), or gauge bosons (W^\pm, Z, γ, H). The search strategy behind this method is to measure the excess of these SM particles inside some large astrophysical systems. However, astrophysical systems present a significant source of uncertainties, making it challenging to infer the presence of Dark Matter. The current ongoing experiments include, Fermi-LAT, MAAGIC, IceCube, etc.

III. Collider Searches

Collider Searches refers to the following process,

$$SM + SM \rightarrow DM + DM + (SM)$$

There are essentially two ways to infer the presence of DM in the context of Collider search:

- **Mono-X** + \cancel{E} / MET, where X refers to γ , Jet, Z or H.
- **Multi-lepton/ Multi-Jet** channel

We look for the missing energy (\cancel{E}) or missing transverse energy (\cancel{E}_T) as a signature for Dark Matter production. The ATLAS and CMS experiments at the Large Hadron A number of such analysis are performed at the ongoing LHC experiments at

CERN. The rest of this thesis is dedicated to the study of single and multicomponent DM search at the proposed International Linear Collider (ILC).

Chapter 3

Effective Field Theory

3.1 Introduction

It is always beneficial to identify the relevant scale of a given physical problem. For instance, the orbits of planets can be accurately calculated without having to worry about their composition. The energy levels of the Hydrogen spectrum can be calculated in quantum mechanics quite precisely without knowing the framework of the SM. One does not need to worry about the effects of the Special Theory of Relativity when tackling a Newtonian problem ($V \ll C$). Thus every theory comes with an intrinsic physical scale - an energy/mass, scale that defines the limit within which the theory is applicable. Beyond this limit, the theory either breaks down or becomes too complex to practically calculate the observable outcomes. [13]

Let us start with an idea for building an effective field theory. Suppose we have a theory that contains two fields, ϕ and ψ with masses m_ϕ and m_ψ respectively, such that, $m_\psi > m_\phi$. Now we want to construct an effective description that only contains the light field ϕ . This can be achieved at energy scales smaller than m_ψ by "integrating out" the heavy field.

$$\mathcal{L}_{\text{full}}(\phi, \psi) \longrightarrow \mathcal{L}_{\text{new}}(\phi) + \mathcal{L}_{\text{effective}}(\phi) \quad (3.1)$$

The effective Lagrangian still contains traces of the heavy field ψ at scales below m_ψ , even though ψ is no longer explicitly present in the Lagrangian. From the above exercise, one could determine the main ingredients needed to construct an EFT Lagrangian. First of all, we need to determine all the relevant degrees of freedom (d.o.f), i.e. the field content of the EFT Lagrangian. We then retain the light fields and "Integrate out" the heavy ones. Second, before writing the EFT Lagrangian, we need to determine the symmetries of the theory. Third, we need

to determine the power counting parameter. The power counting formula δ ¹ is an expansion parameter used to separate out scales. An EFT description comes with three elements. The effective operators \mathcal{O} , their coefficients called Wilson Coefficients C , and the expansion scale Λ . The operator entails the infrared effects (Low energy) \mathcal{O}_{IR} while the Wilson coefficients entail the Ultraviolet effects (High energy), C_{UV} . Based on these, two approaches to EFTs are known: Bottom-Up and Top-Down [14].

- **Top-Down:** In this approach, the fundamental theory often referred to as the UV complete theory of the problem is known. One 'Integrates out' the unneeded heavy degrees of freedom to obtain a low-energy description. In this picture, the Wilson coefficients can be obtained from the UV theory by matching it to the EFT. Some examples of Top-Down approaches are Soft-Collinear Effective Theory and Heavy Quark Effective Theory. [13][14]
- **Bottom-Up:** In this approach, the underlying UV theory is unknown. Assuming that a UV complete theory exists one writes down a set of possible operators consistent with all the relevant symmetries that capture the effects of heavy degrees of freedom. Examples of Bottom-Up approaches are Standard Model Effective Field Theory and Chiral Perturbation Theory. [13] [14]

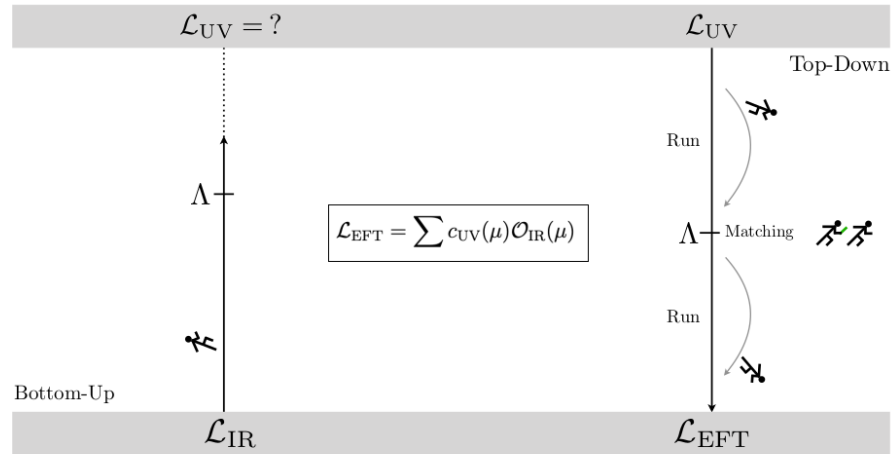


Fig. 3.1 Pictorial representation of Bottom-Up and Top-Down approaches. The image is taken from [14]

The classic textbook example of EFT in action is Fermi's theory of weak decay. In this next section, we give a brief introduction to it. [15]

¹Usually, δ is a ratio of low energy scales such as momentum (P) and short distance scale (Λ), $\delta = \frac{P}{\Lambda}$, $\delta \ll 1$

3.2 Fermi's Theory of Weak Interaction: An EFT example

Almost 30 years before the development of the Electroweak theory, in 1934 Enrico Fermi proposed an idea of four-fermion interaction to explain the β decay process,

$$n \longrightarrow p + e^- + \bar{\nu}_e \quad (3.2)$$

At the time the mediating W boson was not yet discovered. Hence, the four fermi model is a classic example of the Bottom-Up approach valid at energies below the mass of W-boson. However, now we know the UV complete theory which is the theory of weak interactions. In the SM, the weak interaction changes the flavor of the quarks via the mediating W boson which then decays to leptons (see figure).

$$\mathcal{L}_W = \frac{g}{\sqrt{2}} V_{ij} \bar{u}_i \gamma^\mu P_L d_j W_\mu^\pm + \frac{g}{\sqrt{2}} \bar{l} \gamma^\mu P_L \nu_l W_\mu^\pm \quad (3.3)$$

Where, $u_i = u, c, t$ are the up-type quarks, $d_j = d, s, b$ are the down-type quarks, $l = e, \mu, \tau$ and $\nu_l = \nu_e, \nu_\mu, \nu_\tau$ are leptons. V_{ij} is the CKM mixing matrix, $\frac{g}{\sqrt{2}}$ is the coupling constant and $P_L = \frac{1}{2}(1 - \gamma^5)$ is the left handed projection operator. [16] [14]

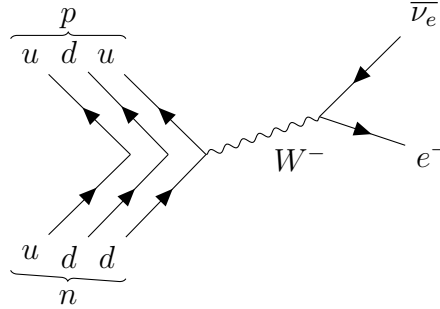


Fig. 3.2 Tree level process for β decay

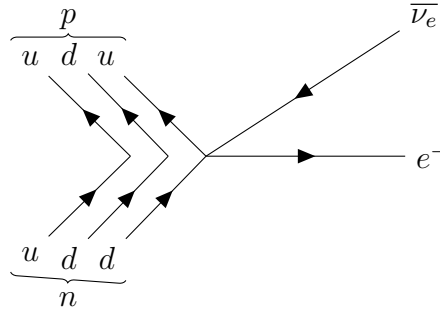


Fig. 3.3 Fermi's effective four fermion vertex for β decay [17]

One can write down the matrix element for the above shown 3.2 process,

$$\mathcal{M} = \left(\frac{ig}{\sqrt{2}} \right)^2 V_{du} (\bar{d} \gamma^\mu P_L u) \left(\frac{-ig_{\mu\nu}}{p^2 - M_W^2} \right) (\bar{e} \gamma^\mu P_L \nu_e) \quad (3.4)$$

In the limit $p^2 \ll M_W^2$, where p is the momentum of the W-boson, the W cannot be kinematically (on-shell) produced. Therefore, Taylor expanding the propagator in this limit,

$$\frac{1}{p^2 - M_W^2} = -\frac{1}{M_W^2} \left(1 + \frac{p^2}{M_W^2} + \frac{p^4}{M_W^4} + \dots \right) \quad (3.5)$$

The EFT expansion parameter δ is $\frac{p^2}{M_W^2}$. Therefore, at leading order (L.O.) the matrix element becomes,

$$\mathcal{M} = \frac{i}{M_W^2} \left(\frac{ig}{\sqrt{2}} \right)^2 V_{du} (\bar{d} \gamma^\mu P_L u) (\bar{e} \gamma^\mu P_L \nu_e) + \mathcal{O} \left(\frac{p^2}{M_W^2} \right) \quad (3.6)$$

The four fermion vertex Lagrangian is written as,

$$\mathcal{L}_{\text{effective}} = -\frac{4G_F}{\sqrt{2}} V_{du} (\bar{d} \gamma^\mu P_L u) (\bar{e} \gamma^\mu P_L \nu_e) \quad (3.7)$$

The Fermi's constant, G_F can be matched the UV complete parameters, g and M_W . In general, the matching demands the UV and the EFT to predict the same IR ($P^2 \ll M_W^2$) results but differ in the UV ($P^2 \gg M_W^2$) limit where on shell production of W boson is possible. The matching of (3.7) and (3.6) leads to,

$$\frac{G_F}{\sqrt{2}} = \frac{g^2}{8M_W^2} \quad (3.8)$$

In this exercise we matched the electroweak theory to the effective description which is the four-fermion interaction. This procedure is called the Top-Down approach. [16] [14]

3.3 DM-SM Effective Field Theory

The SM can be thought of as an EFT of an unknown UV complete BSM theory valid at some scale Λ higher than the validity scale of the SM, i.e. at the electroweak scale, given by VEV, v . In principle, the SM is valid up to the Planck scale, where quantum gravity effects are thought to be taken over but with ample evidence for DM particles and phenomena like non-zero neutrino masses, Hierarchy problems, etc lead us to believe that a scale Λ exists before the Planck scale.[18]

To avoid the overwhelming model-dependent UV complete theories of DM, an EFT approach can be used in the theoretical and Phenomenological study of DM. This approach would capture the effects of new physics in the EFT parameters in a model-independent way. Inspired by Fermi's theory of weak interaction, a DM particle is introduced as an additional degree of freedom that interacts with the SM model particles with some coupling C and is valid up to a scale Λ . Beyond this scale, the EFT description breaks down. The DM-SM interactions can be described in the following way: [18]

$$\mathcal{L}_{\text{int}} = \frac{c_{DM}}{\Lambda^{d+d'-4}} \mathcal{O}_{\text{SM}}^{(d)} \mathcal{O}_{\text{DM}}^{(d')} \quad (3.9)$$

Where, dimensionless quantity c_{DM} denotes the Wilson coefficient, Λ denotes the New Physics scale, $\mathcal{O}_{\text{DM}}^{(d')}$ consists of SM fields with mass dimension d' , while $\mathcal{O}_{\text{SM}}^{(d)}$ consist of SM fields with mass dimension d . The operator $\mathcal{O}_{\text{SM}}^{(d)}$ is invariant under the SM gauge symmetry \mathcal{G}_{SM} while the operator $\mathcal{O}_{\text{DM}}^{(d')}$ is invariant under a dark symmetry \mathcal{G}_{DM} . Where, $\mathcal{G}_{\text{SM}} = SU(3)_C \times SU(2)_L \times U(1)_Y$ while the discrete dark symmetry, $\mathcal{G}_{\text{DM}} = \mathbb{Z}_2$ imposes that DM particles are stable.

$$\mathcal{L}_{\text{DMEFT}} = \mathcal{L}_{\text{SM}} + \mathcal{L}_{\text{int}} + \mathcal{L}_{\text{DM}} \quad (3.10)$$

The above equation (3.10) referees the total Lagrangian including the DM-SM interaction term as described by the EFT and the DM kinetic term. These EFT frameworks can model the DM relic density, direct and indirect searches, and collider production using just three theory parameters: the new physics scale Λ , the DM mass M_{DM} , and the coupling c_{DM} , all in a model-independent manner. In the following two chapters, we consider such a phenomenological study involving a single and two-component Dark Matter scenarios. [18] [19]

Chapter 4

Effective Leptophilic WIMPs

4.1 Introduction

The existence of DM is well motivated by a plethora of astrophysical and cosmological pieces of evidence as already discussed but a ground-based discovery is still awaited. Other than the expected characteristics like charge neutrality, stable DM particle, etc., properties like DM mass and its interactions with the SM particles are yet to be found. Therefore we must introduce a DM particle as an extension of the SM. There are two ways for BSM theoretical and phenomenological studies: UV complete models and an EFT approach. Having already discussed the advantages of an EFT approach, we will introduce a set of EFT operators describing DM-SM interactions and study its detectability at the International Linear Collider i.e. an e^+e^- machine.[\[20\]](#)

In the context of a collider, the DM particle is missed in the detector. However, its production can be inferred through a Mono-X signal, typically initiated by radiation (such as a photon γ or jets). In the study of DM EFT at colliders, it's crucial to ensure that the center-of-mass energy (\sqrt{s}) remains below the scale of New Physics (Λ). This constraint cannot be guaranteed in a hadron collider like the LHC, where the partonic center-of-mass energy (\sqrt{s}) is unknown. However, lepton colliders such as the ILC offer distinct advantages, including known center-of-mass energy, symmetric beams, and the capability to polarize beams to reduce Standard Model background contributions. These features make DM EFT studies more feasible with e^+e^- machines compared to proton-proton collisions at the LHC. Building upon this, our study delves into DM EFT within the context of e^+e^- colliders, assuming the DM to be a Dirac fermion that interacts favorably with Standard Model leptons.

4.2 DM-SM Effective Operators

Having already discussed about the general idea of DM-SM EFT operators in the last chapter (refer to (3.9)) we now introduce dimension 5 and dimension 6 effective operators considering DM to be a Dirac fermion χ and which transforms under a dark symmetry, $\mathcal{G}_{\text{DM}} = \mathbb{Z}_2$.

Dimension 5 Operators	
Name	Description
\mathcal{O}_{D1}^5	$\frac{c_{B1}}{\Lambda} (\bar{\chi} \sigma_{\mu\nu} \chi) B^{\mu\nu}$
\mathcal{O}_{D2}^5	$\frac{c_{B2}}{\Lambda} (\bar{\chi} \sigma_{\mu\nu} \gamma^5 \chi) B^{\mu\nu}$
\mathcal{O}_3^5	$\frac{c_{H1}}{\Lambda} (\bar{\chi} \chi) (H^\dagger H)$
\mathcal{O}_4^5	$\frac{c_{H2}}{\Lambda} (\bar{\chi} \gamma^5 \chi) (H^\dagger H)$

Table 4.1 Here, χ is a DM fermion, $B^{\mu\nu}$ ³ refers to $U(1)_Y$ gauge field strength tensor, H stands for the SM Higgs doublet, and $\sigma_{\mu\nu}$ ⁴ refers to the Pauli spin matrices, describing the spin of particles.[20]

Dimension 6 Operators			
Leptophilic	Description	Hadrophilic	Description
\mathcal{O}_{DL}^6	$\frac{c_{l1}}{\Lambda^2} (\bar{\chi} \gamma_\mu \chi) (\bar{l} \gamma^\mu l)$	\mathcal{O}_{DQ}^6	$\frac{c_{q1}}{\Lambda^2} (\bar{\chi} \gamma_\mu \chi) (\bar{q} \gamma^\mu q)$
\mathcal{O}_L^6	$\frac{c_{l2}}{\Lambda^2} (\bar{\chi} \gamma_\mu \gamma^5 \chi) (\bar{l} \gamma^\mu l)$	\mathcal{O}_Q^6	$\frac{c_{q2}}{\Lambda^2} (\bar{\chi} \gamma_\mu \gamma^5 \chi) (\bar{q} \gamma^\mu q)$
\mathcal{O}_{L1}^6	$\frac{c_{l3}}{\Lambda^2} (\bar{\chi} \gamma_\mu \gamma^5 \chi) (\bar{l} \gamma^\mu \gamma_5 l)$	\mathcal{O}_{Q1}^6	$\frac{c_{q3}}{\Lambda^2} (\bar{\chi} \gamma_\mu \gamma^5 \chi) (\bar{q} \gamma^\mu \gamma_5 q)$
\mathcal{O}_{DL}^6	$\frac{c_{l4}}{\Lambda^2} (\bar{\chi} \gamma_\mu \chi) (\bar{l} \gamma^\mu \gamma_5 l)$	\mathcal{O}_{DQ}^6	$\frac{c_{q4}}{\Lambda^2} (\bar{\chi} \gamma_\mu \chi) (\bar{q} \gamma^\mu \gamma_5 q)$

Table 4.2 Here, l stands for either left handed doublet(LH) or right handed (RH) singlet SM lepton. q stands for LH doublet or RH singlet SM quarks of all flavours and χ denotes the DM fermion.[20]

The operators involving the field strength tensor $B^{\mu\nu}$ are classified as Loop generated operators (LG) because their interaction with DM is at least in one loop level via NP in a perturbative UV theory. Thus, operators, \mathcal{O}_{D1}^5 and \mathcal{O}_{D2}^5 will have a smaller contribution. The rest of the operators are classified as potential tree generated (PTG).

While Hadrophilic operators can be thought of in the context of the LHC and are prone to direct search constraints, Leptophilic operators can be probed at the ILC and can hide from the null result from the direct search experiments. We have already talked about the advantages of the ILC machine over the LHC. Therefore, we will be now concerned with all the Dimension 6 ⁵ Leptophilic operators mentioned in the table 4.2. [21]

4.3 DM Constraints

Using current experimental limits from DM searches, the initial exercise is to find constraints on these operators. These mostly consist of relic density, direct search, and indirect searches. The DM relic density value from the CMB measurements provides the most stringent bound for the EFT parameters, Λ , C , and mass of the DM, M_{DM} . The direct search experiments look for DM-nucleon scattering to get a signature of DM particle. Leptophilic DM, by definition, does not have direct interaction with quarks. However, the coupling of DM with quarks will come at a one-loop level, where the loop can be of charged leptons coupled to DM. This is depicted in the figure below. The presence of DM can also be inferred via the excess of photons γ or particles ($l\bar{l}$) from an astrophysical source. FermiLAT and Cherenkov Telescope Array (CTA) are such experiments looking for Indirect signatures of DM. Direct search and Indirect search bounds are not explored in this thesis. We will address relic density constraints followed by DM signal at e^+e^- collider in subsequent sections. The Benchmark Points (BP) are taken from "Effective Leptophilic WIMPs at e^+e^- collider" [20] and taken care of constraints from all three measurements.

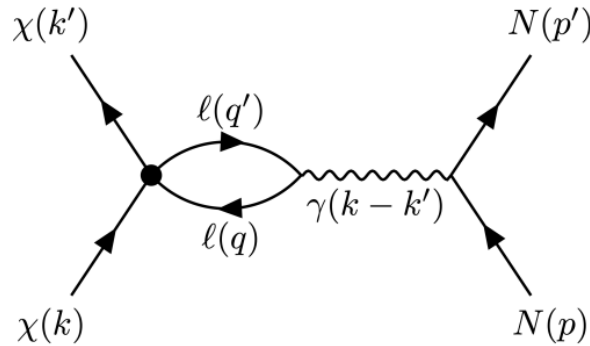


Fig. 4.1 DM-nucleon scattering via one loop coupling with leptons. The image is taken from paper

⁵As Higgs have a very small coupling with SM leptons, we will neglect dimension 5 Higgs portal interaction terms in the context of ILC

4.3.1 Relic Density

Assume χ as a WIMP-like Dirac fermion, which was in both thermal and chemical equilibrium with the Standard Model (SM) particles during the early universe. However, at some later epoch when the universe expanded and cooled down, departure from thermal equilibrium led to constant DM relic density. The solution to the Boltzmann equation gives the relic density for WIMP-like DM. This is calculated in the Appendix (refer WIMP). [10] [11]

$$\frac{dY}{dt} = -\frac{\lambda}{x^{n+2}}[Y^2 - (Y^{eq})^2] \quad (4.1)$$

Where, λ is given as,

$$\lambda = 0.264 \frac{g_{*s}}{\sqrt{g_*}} m_{pl} m_{DM} \sigma_0 \quad (4.2)$$

Here, $x = m_{DM}/T$ (T : Temperature), $Y = n/s$ refers to DM yield where n is the DM density and s is the entropy density. m_{pl} denotes the Planck mass. σ_0 denotes the temperature-independent cross section given by, $\sigma_0 = \langle \sigma_{\chi+\bar{\chi} \rightarrow l+\bar{l}} |v| \rangle x^n$. Where $\langle \sigma_{\chi+\bar{\chi} \rightarrow l+\bar{l}} |v| \rangle$ is the thermal average cross-section times velocity of the DM annihilation process to leptons. In the non-relativistic regime ($x \gg 3$) resulting in Cold Relic, the equilibrium value of the number of χ 's per co-moving volume takes the form, [11]

$$Y^{eq}(x) = 0.145 \frac{g_{DM}}{g_*} x^{3/2} e^{-x} \quad (4.3)$$

Here, g_{DM} refers to number of DM internal states and g_* is the effective massless degrees of freedom. Now we consider an operator \mathcal{O}_{DL}^6 for a certain process, $\chi\bar{\chi} \rightarrow e^+e^-$ and look for the evolution of (4.1) by varying EFT parameter Λ , New physics scale and C , Wilson Coefficient.

The relic abundance is the mass density of the species in terms of the critical density in a co-moving volume. It is given as, $\Omega_{DM} = \rho/\rho_c$, where ρ denotes the DM density and ρ_c denotes the critical density. The measured value of the relic density obtained from Planck data is then compared to the obtained model value. Where the observed Planck data value is, [12]

$$\Omega h^2 = 0.11933 \pm 0.00091 \quad (4.4)$$

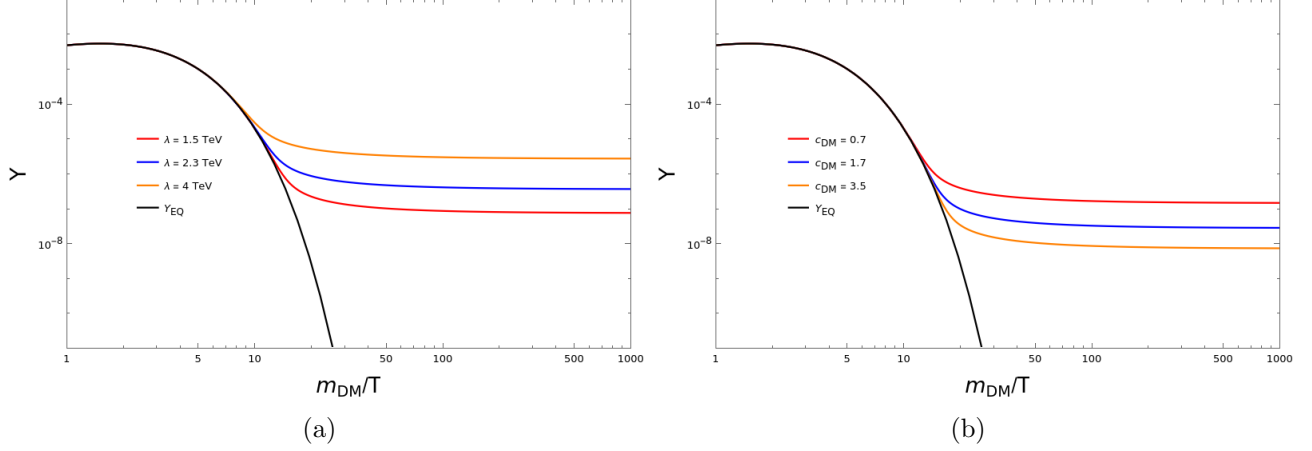


Fig. 4.2 (a) Evolution of yield keeping $(m_{DM}, c) = (300 \text{ GeV}, 1)$ fixed and varying New physics scale, $\Lambda = (1.5, 2.3, 4) \text{ TeV}$. (b) Varying Wilson coefficient, $c = (0.7, 1.7, 3.5)$ while keeping $(m_{DM}, \Lambda) = (300 \text{ GeV}, 3 \text{ TeV})$ fixed

As shown in the above figure, the Blackline refers to the equilibrium yield. The freeze-out occurs at $x_f = m_{DM}/T_f$, where T_f is the freeze-out temperature. We can see the variation in yield for values of $\Lambda = (1.5, 2.3, 4) \text{ TeV}$ (a) and $c = (0.7, 1.7, 3.5)$ at freeze-out.

We use the Planck data (4.4) to constrain our parameter space. That is to consider the value of m_χ and Λ which gives the correct relic density number. The Leptophilic operators described above are written in **FeynRules** [22] and **LanHEP** [23] as an extension of the SM Lagrangian. The model file is then fed to **MicrOMEGAS** [24] to get constraints on our EFT parameters. Λ and m_χ are scanned in a range of:

$$\Lambda : \{1 - 10^4 \text{ GeV}\}; m_\chi : \{1 - 10^4 \text{ GeV}\} \quad (4.5)$$

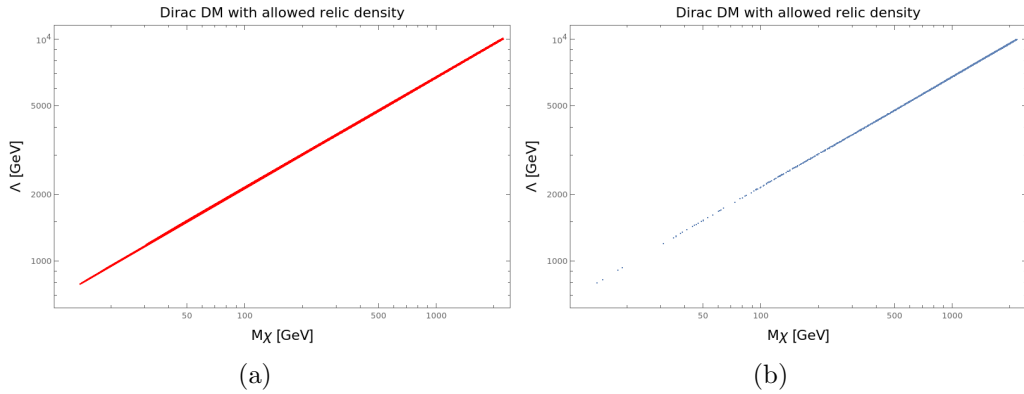


Fig. 4.3 Two parameters, the new physics scale Λ and DM mass M_χ varied in the range of $1 - 10^4$ with all the operators combined $(c_{l1}, c_{l2}, c_{l3}, c_{l4}) = (1, 1, 1, 1)$

The new physics scale, $\Lambda > m_\chi/(2\pi)$, is required for the effective field theory (EFT) prescription to be valid. We observe from the above plots that as the DM mass is increased, the new physics scale Λ also rises to satisfy the relic density constraints as the relic density of thermal WIMPs is given by, $\Omega_\chi h^2 \approx 1/\langle\sigma V\rangle \approx \Lambda^4/m_\chi^2$. [20] We now take the Benchmark points that satisfy DM relic density, direct search, and Indirect search constraints from the paper. These points are further fed to the collider search in the next section.

Benchmark Point	Model	m_χ (GeV)	Λ (GeV)
BP1	(1,1,1,1)	350	2800
BP2	(1,1,1,1)	400	3000

Table 4.3 Benchmark Points for Dirac DM scenario. Here, Model refers to choices of Wilson coefficients.

4.4 Collider search

It is quite clear that Leptophilic DM operators in the context of the LHC have very suppressed cross-sections due to one loop production (refer 5.1). ILC on the other hand offers two advantages: 1) Known CM \sqrt{s} energy. 2) The ability to polarize e^+e^- beams to reduce the SM background. The classic DM signature comes in the form of missing energy as DM is invisible to the detector. Thus, one must depend on one or more initial state radiation (ISR) photons from one of the legs of leptons. In this scenario, the signal is mostly provided by,

$$e^+ + e^- \rightarrow \chi\bar{\chi} + \gamma \rightarrow ME + \gamma; \quad (4.6)$$

where ME stands for missing energy carried away by DM particles. We should keep in mind that events with more than one photon will be highly suppressed. Therefore, Mono-photon events with ME are a classic signature of DM production at e^+e^- collider. To pair produce DM at the collider, one must ensure that $\sqrt{s} > 2m_\chi$. Therefore, from BP 4.3, it is suitable to probe Dirac DM at CM energy \sqrt{s} of 1 TeV.

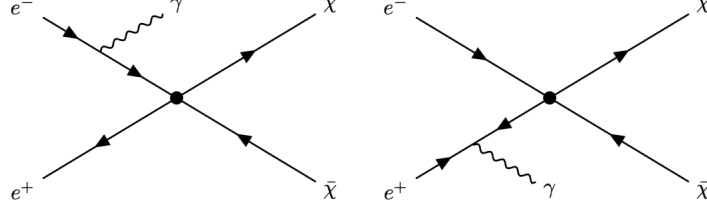


Fig. 4.4 Initial State Radiation (ISR) with DM pair production. Here, the blob represents the effective DM-SM vertex. [20]

4.4.1 DM production cross section

The use of beam polarization can be helpful to increase the DM signal and reduce the relevant background. The beam polarization (P_{e^-/e^+})⁶ refers to longitudinal polarization containing a mixture of left-handed (n_L) and right-handed (n_R) e^-/e^+ . The generic expression for the differential cross-section of the process, $e^+e^- \rightarrow \chi\bar{\chi}$ is given by, [20]

$$\begin{aligned} \frac{d\sigma(P_e^-, P_e^+)}{d\Omega} = \frac{1}{4} & \left((1 + P_{e^-})(1 + P_{e^+}) \left(\frac{d\sigma}{d\Omega} \right)_{RR} + (1 - P_{e^-})(1 - P_{e^+}) \left(\frac{d\sigma}{d\Omega} \right)_{LL} \right. \\ & \left. + (1 + P_{e^-})(1 - P_{e^+}) \left(\frac{d\sigma}{d\Omega} \right)_{RL} + (1 - P_{e^-})(1 + P_{e^+}) \left(\frac{d\sigma}{d\Omega} \right)_{LR} \right) \end{aligned} \quad (4.7)$$

Taking advantage of the initial beam polarization as mentioned before we plot the variation of DM production cross section $\sigma_{e^+e^- \rightarrow \chi\bar{\chi}}$ varying \sqrt{s} , m_χ , Λ , and couplings, c_{l_i} . Different choices of beam polarization are as follows:

$$\begin{cases} P_{e^-} : P_{e^+} = 0, 0 \\ P_{e^-} : P_{e^+} = +0.8, -0.3 \\ P_{e^-} : P_{e^+} = -0.8, +0.3 \end{cases} \quad (4.8)$$

The concerned operators are written in **FeynRules** [22] and **LanHEP** [23] as an extension of the SM Lagrangian. The model file is then fed to **Madgraph5** [25] for event generation.

⁶ $P_{e^-/e^+} = \frac{n_R - n_L}{n_R + n_L}$

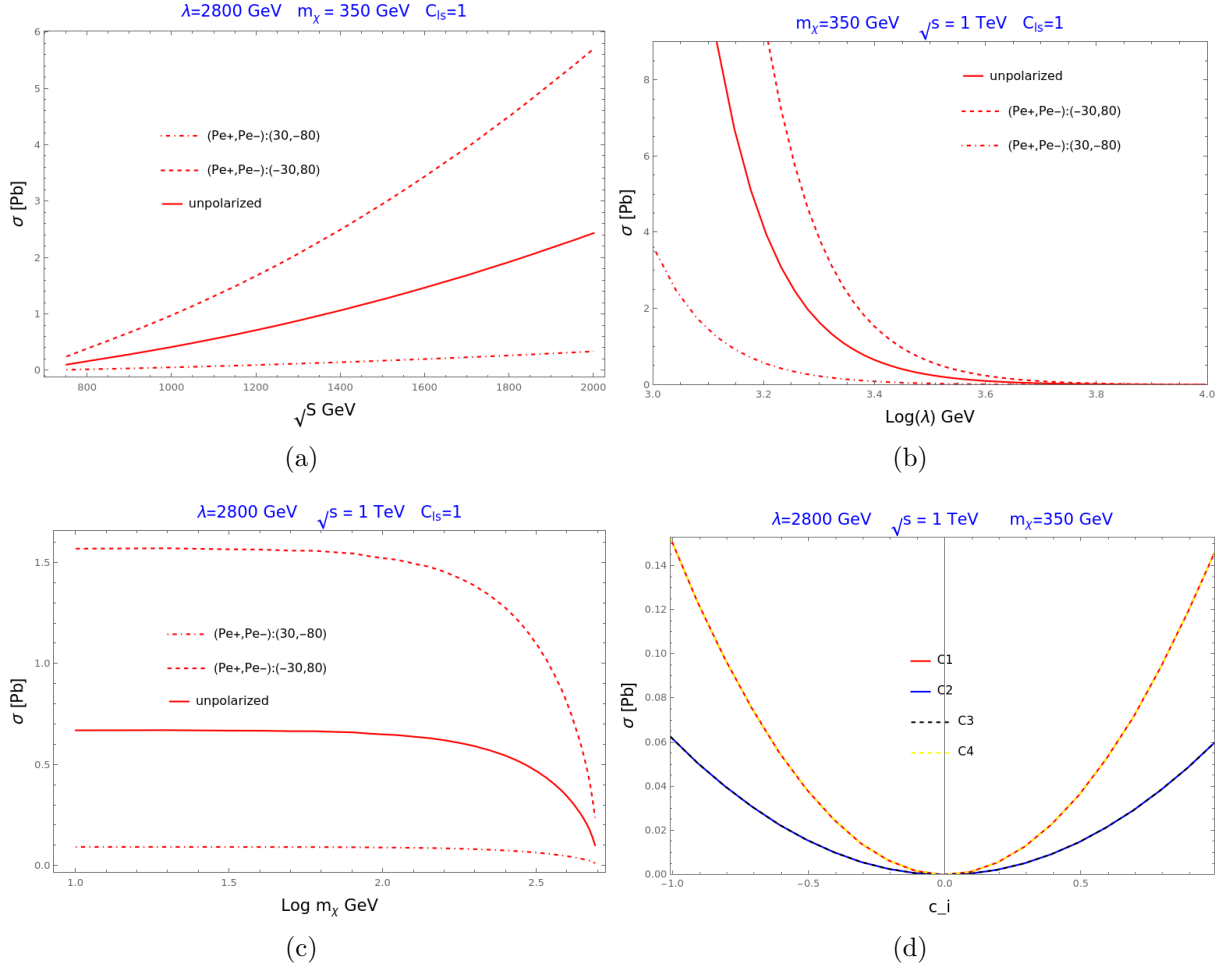


Fig. 4.5 Variation of $\sigma_{e^+e^- \rightarrow \chi\bar{\chi}}$ as a function of \sqrt{s} (a), Λ (b), m_χ (c) and couplings, c_{l_i} (d) for Dirac DM (BP1) for three different choices of beam polarization.

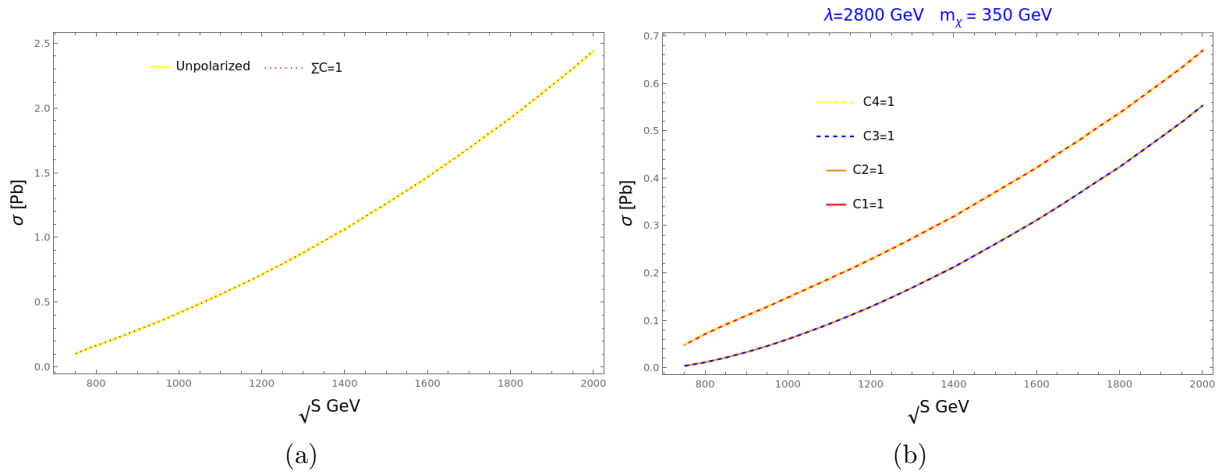


Fig. 4.6 a) Adding cross-section of all C_{l_i} individually and comparing it with all taken at once for unpolarized beam. (b) Individual C_{l_i} variation of cross-section with CM energy \sqrt{s}

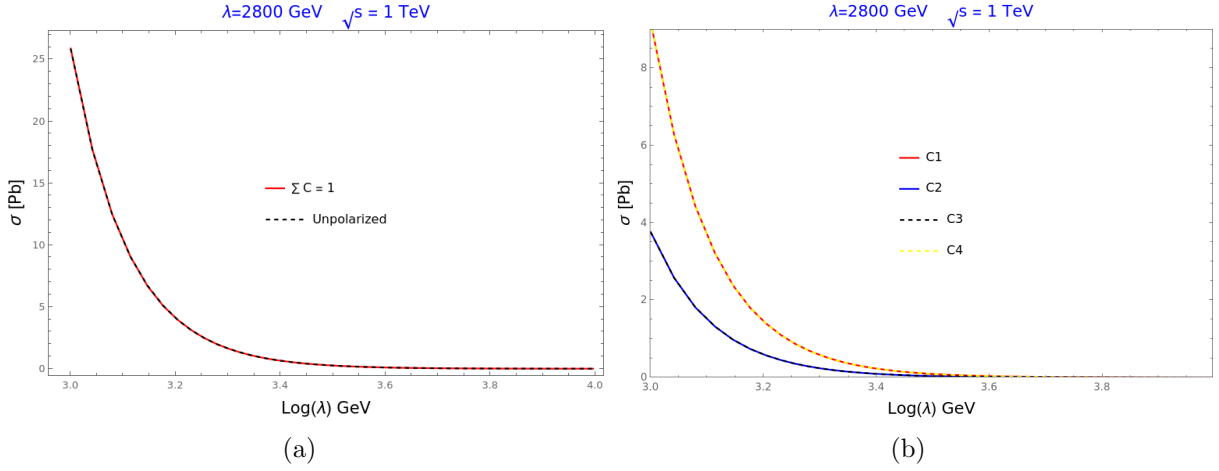


Fig. 4.7 (a) Adding cross-section of all C_i individually and comparing it with all taken at once for unpolarized beam. (b) Individual C_i variation of cross-section with $\text{Log}\Lambda$

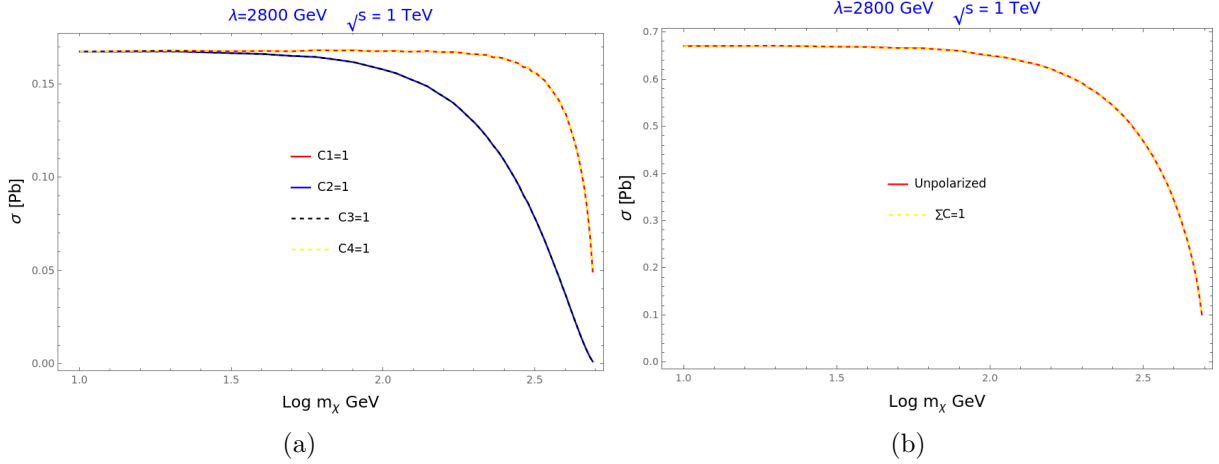


Fig. 4.8 (a) Adding cross-section of all C_i individually and comparing it with all taken at once for unpolarized beam. (b) Individual C_i variation of cross-section with $\text{Log}m_\chi$

From figure 4.5 we find that the cross section increases with \sqrt{s} up to EFT limit $\Lambda > \sqrt{s}$ (a). Here all Wilson coefficients are set to unity. On the other hand, the cross-section falls with Λ as $\sigma \propto (1/\Lambda^2)^2$ for a fixed value of \sqrt{s} and m_χ as mentioned on top of (b). It is also interesting to note that the cross-section remains constant up to some value of m_χ and then falls off as expected, $\sqrt{s} < 2m_\chi$ (c). Lastly, the values of Wilson coefficients are varied in a range of (-1,1) (d). Our signal of interest at collider is one with a mono photon event i.e. $e^+e^- \rightarrow \chi\bar{\chi}\gamma$. Here, the DM will be missed inside the detector and one could infer its presence via the mono-photon event. But the background $e^+e^- \rightarrow \nu\bar{\nu}\gamma$ will also be present and neutrinos will also be missed in the detector mimicking the presence of DM. Hence,

one needs to extract the signal from the background by constructing appropriate observables and applying necessary cuts to separate the SM background events from the signal.

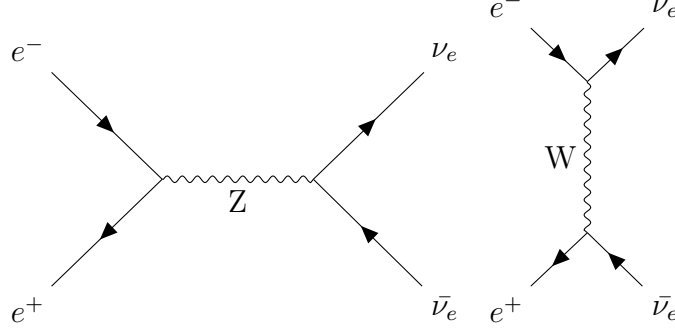


Fig. 4.9 s and t channel Feynman diagrams for the SM background process, $e^+e^- \rightarrow \nu_e\bar{\nu}_e$. Mono-photon events will arise from ISR [17]

Beam Polarization		Signal ($\sigma_{e^+e^- \rightarrow \chi\bar{\chi}\gamma}$) (fb)		Background ($\sigma_{e^+e^- \rightarrow \nu_e\bar{\nu}_e\gamma}$) (fb)
P_{e^+}	P_{e^-}	BP1	BP2	
0	0	15.96	8.47	2380
0.3	-0.8	2.24	1.18	5570
-0.3	0.8	37.39	19.84	360

It is clear from the table 4.4.1 that the third choice of beam polarization $(P_e^+, P_e^-) = (-0.3, 0.8)$ maximizes the signal and reduces the background significantly. The next subsection provides a brief overview of some observables.

4.4.2 Event Distributions

The parton-level signal and background events are generated for the Benchmark points 4.3 using Monte Carlo event generator **MadGraph5** [25]. The event file is then fed to **Pythia8** [26] for Parton showering and **Delphes** [27] for detector-level simulation. The observables Missing Energy \cancel{E} , Missing Transverse Energy MET, missing mass m_{mass} and Photon Energy E_γ are constructed for Benchmark points, BP1: $(m_\chi, \Lambda) = (350, 2800)$, BP2: $(m_\chi, \Lambda) = (400, 3000)$ and Background $\nu_e\bar{\nu}_e\gamma$ at CM energy $\sqrt{s} = 1TeV$. The definitions of observables are discussed in the Collider kinematics chapter. [20]

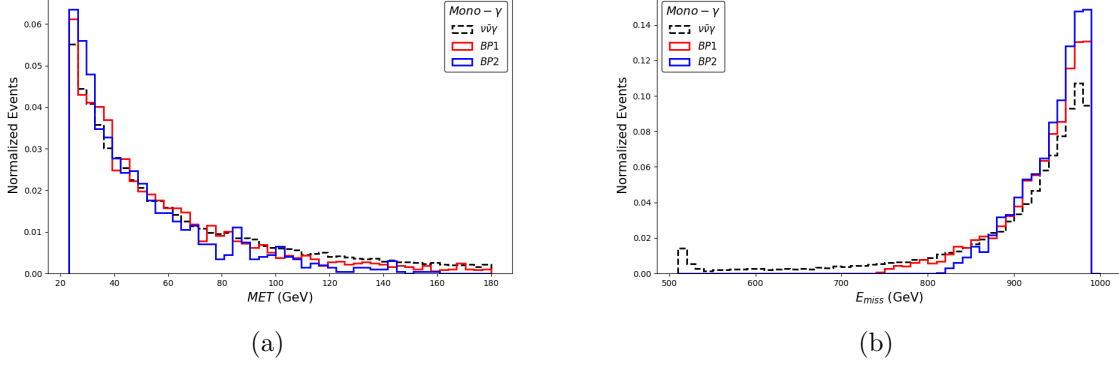


Fig. 4.10 a) Normalized mono- γ distribution for the BP1, BP2, and background as a function of missing transverse energy (MET) (b) Normalized mono- γ distribution for the BP1, BP2, and background as a function of missing energy (E_{miss})

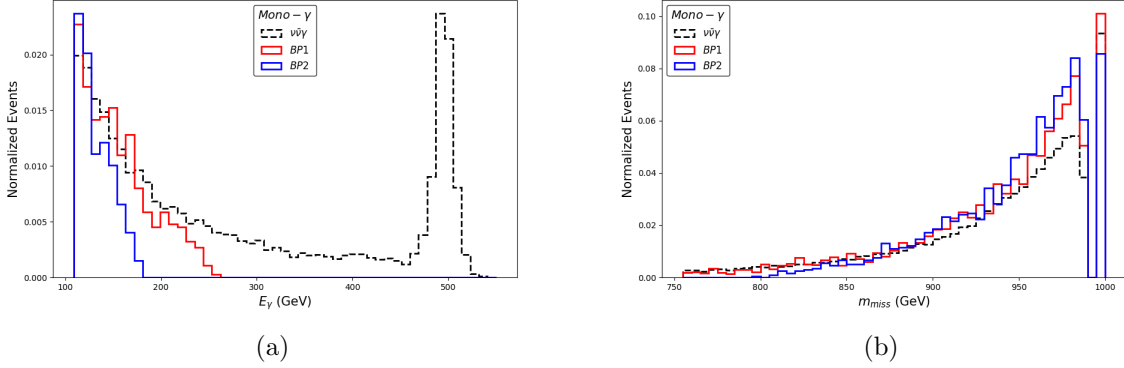


Fig. 4.11 a) Normalized mono- γ distribution for the BP1, BP2, and background as a function of photon energy E_γ (b) Normalized mono- γ distribution for the BP1, BP2, and background as a function of missing mass (m_{miss})

The E_γ distribution clearly shows a distinction of signal from the SM neutrino background. Hence, by applying appropriate cuts we could define the efficiency factor $\epsilon = \frac{S}{B}$ and the signal significance, $\sigma = \frac{S}{\sqrt{S+B}}$, where, S refers to the signal events for a given Luminosity after each cut ($S = \sigma_S \mathcal{L}$) and B refers to the background events for a given Luminosity after each cut ($B = \sigma_B \mathcal{L}$).

4.4.3 Summary and Conclusion

This work is based on the paper "*Effective Leptophilic WIMPs at the e^+e^- collider*" [20]. A model-independent EFT study of DM has been studied due to the unknown nature of DM. We discussed two types of DM-SM dimension 6 operators, Hadrophilic and Leptophilic. While direct interaction of quarks with DM is prone to direct search and the LHC, the EFT validation in the context of the LHC is

questionable. Leptophilic DM on the other hand can be probed at the ILC abiding by the EFT limit and at least one loop with SM quarks for direct search constraints. We then take the Benchmark points that satisfy Dirac DM relic density, direct search, and indirect search constraints.

The mono γ events with missing energy provide a classic signature of DM pair production. However the SM background, $\nu\nu\gamma$ could give a false signal as neutrinos will be missed in the detector as well. The SM background can be reduced significantly by choosing the right beam polarization, $(P_e^+, P_e^-) = (-0.3, 0.8)$ and by applying appropriate cuts to the observables such as missing energy \cancel{E} , MET, m_{miss} and E_γ . In the next chapter, we address a completely different question of distinguishing two DM components at e^+e^- collider. [28]

Chapter 5

Mono-X signal and Two Component DM

5.1 Introduction

Cosmological observations suggest that ordinary matter makes up 5% of the universe and that includes at least three distinct fundamental interactions as well as seventeen different species. Therefore, it seems improbable that dark matter, which makes about 25% of the universe, is composed of just one species. Motivated from this simple fact we investigate the study of two DM components belonging to two different "dark sectors". Multicomponent DM frameworks provides a rich phenomenology like coupled Boltzmann equations to determine relic contribution, interactions between DM components, modified Freeze-out/Freeze-In, modified Direct search and Indirect search constraints, large allowed parameter space, etc. [29]

We introduce two dark sector particles as an addition to the SM particles. They transform under a dark symmetry $\mathcal{G}_{\text{DM}} = \mathbb{Z}_2$. Thus the complete symmetry, $\mathcal{G}_{\text{SM}} \times \mathcal{G}_{\text{DM}}$ is followed. There are essentially two classes of divisions to infer the presence of DM in the context of Collider search: [30]

- **Mono-X** + \cancel{E} / MET, where X refers to γ , Jet, Z or H.
- **Multi-lepton/ Multi-Jet** channel

Mono-X signal as already discussed in the last chapter arises when two DM particles are pair produced directly with an ISR signal. Multi-lepton or Multi-Jet can be thought of as n-leptons + m-jets + A-photons + \cancel{E} arises when DM is associated with a "Heavier Dark Sector Particles (HDSP)". Decay of such a Heavy partner into DM and multi-lepton/jet channel can be studied. In any case peaks/bumps in missing energy \cancel{E} or MET distributions provide a way to identify the presence

of DM as we have already seen in the last chapter. However, now we want to distinguish the two peaks coming from two DM components.

An e^+e^- collider is more preferred for distinguishing two WIMP-like DM particles as compared to the LHC. This is due to the following reasons:

- The possibility of using observables such as missing energy \cancel{E}
- The availability of longitudinal momentum
- Advantage of using beam polarization can significantly reduce the SM background
- Know CM energy \sqrt{s}

5.2 DM effective Operatos

Identifying and separating two WIMP DM components at colliders is a challenging task as the main signal of both DM components is of the mono-X type ($X = \gamma, Z, H$). Having discussed about the advantages of e^+e^- machine, we present a model-independent study with DM-SM EFT operators where DM1, (φ) is a scalar type and DM2, (χ), is a fermion type, and they interact favorably with SM leptons and SM force carriers. [28]

Type	Name	Operator
φ	\mathcal{O}_s^1	$\frac{1}{\Lambda^2} L \Phi l_R (\varphi^2)$
φ	\mathcal{O}_s^2	$\frac{1}{\Lambda^4} (L D_\mu \Phi l_R) (\varphi \partial^\mu \varphi)$
φ	\mathcal{O}_s^3	$\frac{1}{\Lambda^2} (B_{\mu\nu} B^{\mu\nu} + W_{\mu\nu} W^{\mu\nu}) (\varphi^2)$
χ	\mathcal{O}_f^1	$\frac{1}{\Lambda^2} (\bar{L} \gamma^\mu L + \bar{l}_R \gamma^\mu l_R) (\bar{\chi} \gamma_\mu \chi)$
χ	\mathcal{O}_f^2	$\frac{1}{\Lambda^3} (L \Phi l_R) (\bar{\chi} \chi)$
χ	\mathcal{O}_f^3	$\frac{1}{\Lambda^3} (B_{\mu\nu} B^{\mu\nu} + W_{\mu\nu} W^{\mu\nu}) (\bar{\chi} \chi)$

Table 5.1 φ is a scalar DM and χ is a fermionic DM, $L(l_R)$ is the left (right)-handed SM lepton doublet (singlet), $B_{\mu\nu}$ and $W_{\mu\nu}$ are the electroweak field strength tensors, Φ is the SM Higgs doublet, D_μ is the gauge-covariant derivative, and Λ is the new physics (NP) scale of the EFT operators.

The interaction of DM particles with SM particles can happen via $2 \rightarrow 3$ hard scattering or $2 \rightarrow 2$ scattering with Initial state radiation of $X = (\gamma, Z, H)$ from one of the legs of leptons. The corresponding Feynman diagram is shown below,

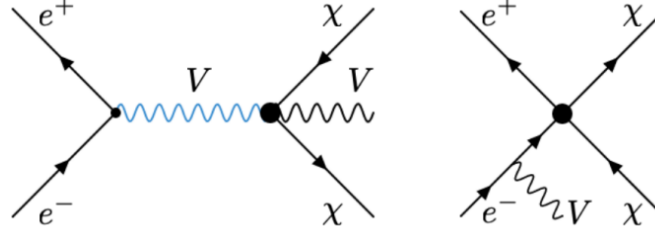


Fig. 5.1 Feynman diagram corresponding to Mono-X signal and DM pair production with effective vertex represented by blob. Here, V represents γ, Z, H [28]

$$e^+ + e^- \rightarrow \chi\bar{\chi} + X \rightarrow ME + X \quad (5.1)$$

$$e^+ + e^- \rightarrow \varphi\varphi + X \rightarrow ME + X; \quad (5.2)$$

Our study primarily focuses on the pursuit of identifying double bumps in \cancel{E} distributions resulting from two DM components. But the question arises, Will there always be a two-peak behaviour? The peaks/bumps in the \cancel{E} distribution depend on Kinematics and Dynamics. Kinematics governs the peak position in \cancel{E} which depends on CM energy \sqrt{s} and DM mass, while the shape of the distribution is determined by Dynamics which is governed by the operator structure. Whether the bump-hunting approach is effective for a particular operator depends on the following principles: [28]

- Angular Momentum conservation
- Rotational invariance in Minkowski space
- Collinear divergence
- Operator structure
- DM mass: m_{DM} determines the peak position in \cancel{E} and sizes of the peaks which in turn depends on the coupling c , New Physics scale Λ and DM mass.

5.3 Collider Analysis

We began this section by looking at the combination of operators that give a two-peak behavior in the \cancel{E} distribution. We then look at the contribution of $\nu\nu X$ background covering one of the two peaks. In the following subsection we introduce an observable, called, the plot of bin-wise statistical significance (\sqrt{S}/B) in the \cancel{E} distribution which evokes the presence of the hidden peak.

5.3.1 \cancel{E} of Individual Operators

A double hump distribution in \cancel{E} , may arise from specific combinations of operators. One operator generates a peak in the higher \cancel{E} region, while the other creates a peak in the \cancel{E} region. This is often due to factors like angular momentum conservation, collinear divergence etc as mentioned earlier. Typically, when one operator contributes via initial state radiation and the other emits a vector boson from the vertex, they combine to produce two distinct peak signals.[5.1](#)

We now identify specific combinations of each operator leading to this double peak behavior for two-DM candidates. The blue and red colors represent two different DM candidates, χ and φ interacting via different operators [5.1](#). We include examples of each mono-X ($X = \gamma, Z, H$) channels. [\[28\]](#)

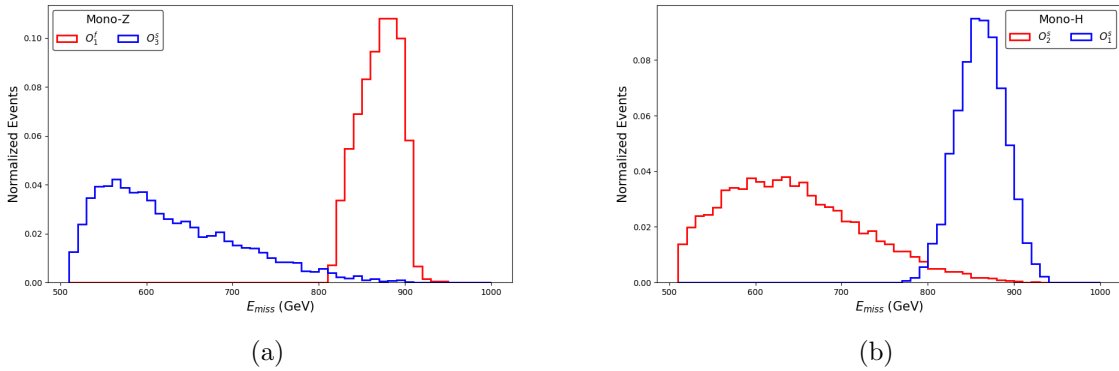


Fig. 5.2 Two peak behavior combinations. Individual Normalized \cancel{E} distributions for mono-Z and mono-H signals arising from operators: (a) \mathcal{O}_1^f and \mathcal{O}_3^s (b) \mathcal{O}_2^s and \mathcal{O}_1^f . Here, the masses of DM candidates are chosen to be 100 GeV (\mathcal{O}_2^s and \mathcal{O}_3^s) and 400 GeV (\mathcal{O}_1^s and \mathcal{O}_1^f). We choose $\Lambda = 1.2\text{TeV}$, $\sqrt{s} = 1\text{ TeV}$ with $(P_e^+, P_e^-) : (+30\%, +80\%)$

Figure [5.2](#) shows mono-Z and mono-H signals. We have reconstructed Z and H in l^+l^- ($l = e, \mu$) and $b\bar{b}$ decay channels respectively.

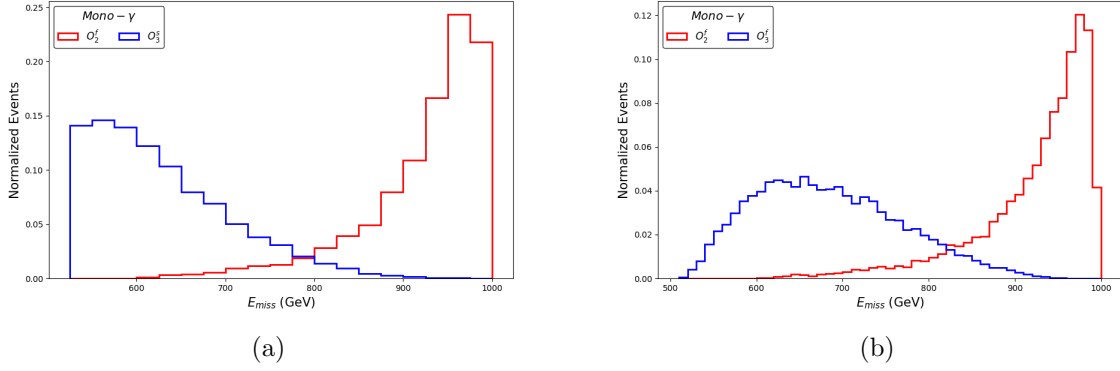


Fig. 5.3 Two peak behavior combinations. Individual Normalized \cancel{E} distributions for the mono- γ signal arising from operates: (a) \mathcal{O}_3^s and \mathcal{O}_2^f (b) \mathcal{O}_3^f and \mathcal{O}_2^f . Here, the masses of DM candidates are chosen to be 100 GeV (\mathcal{O}_3^s and \mathcal{O}_3^f) and 200 GeV (\mathcal{O}_2^f). We choose $\Lambda = 1.2\text{TeV}$, $\sqrt{s} = 1\text{ TeV}$ with $(P_e^+, P_e^-) : (+30\%, +80\%)$

In the next subsection we talk about the SM background. In the process, $e^+e^- \rightarrow \nu\nu X$, where $X = \gamma, Z, H$ the neutrinos will be missed in the detector mimicking the presence of DM.

5.3.2 Signal and Background

At e^+e^- collider the s and t channel processes, $e^+e^- \rightarrow \nu\nu X$ will have a higher production cross-section than the signal. For instance, at $\sqrt{s} = 1\text{ TeV}$ with beam polarization $(P_e^+, P_e^-) : (+30\%, +80\%)$, the SM background contributes the following: $\nu\nu\gamma$: 640 fb, $\nu\nu Z$: 16 fb, $\nu\nu H$: 46 fb.

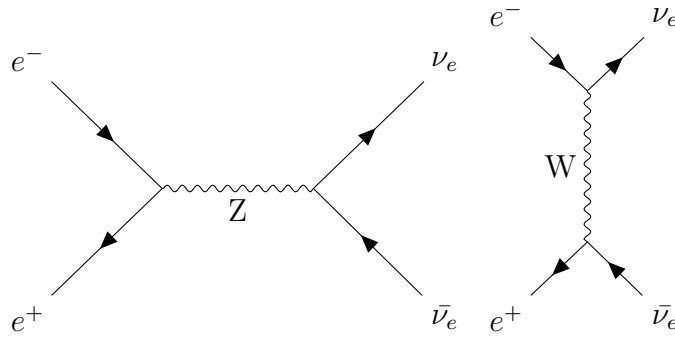


Fig. 5.4 s and t channel Feynman diagrams for the SM background process, $e^+e^- \rightarrow \nu_e \bar{\nu}_e$. Mono-X events will arise from ISR [17]

In the previous subsection we have seen that a particular combination of operators gives rise to two peak behavior in the \cancel{E} distribution. Now we again look for mono-X signal in \cancel{E} distributions together with the SM background.

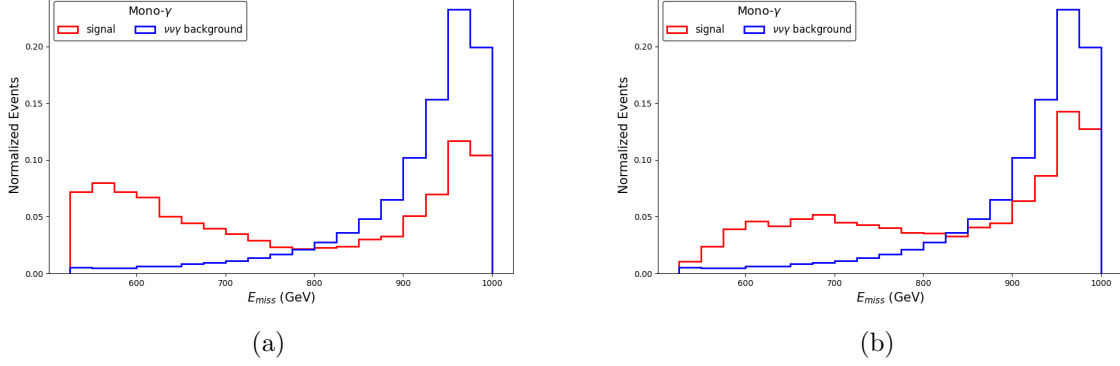


Fig. 5.5 Signal together with background $\nu\nu\gamma$. Normalized \cancel{E} distributions for the mono- γ signal arising from operates: (a) \mathcal{O}_3^s (100 GeV) and \mathcal{O}_2^f (200 GeV) (b) \mathcal{O}_3^f (100 GeV) and \mathcal{O}_2^f (200 GeV). We choose $\Lambda = 1.2\text{TeV}$, $\sqrt{s} = 1\text{ TeV}$ with $(P_e^+, P_e^-) : (+30\%, +80\%)$

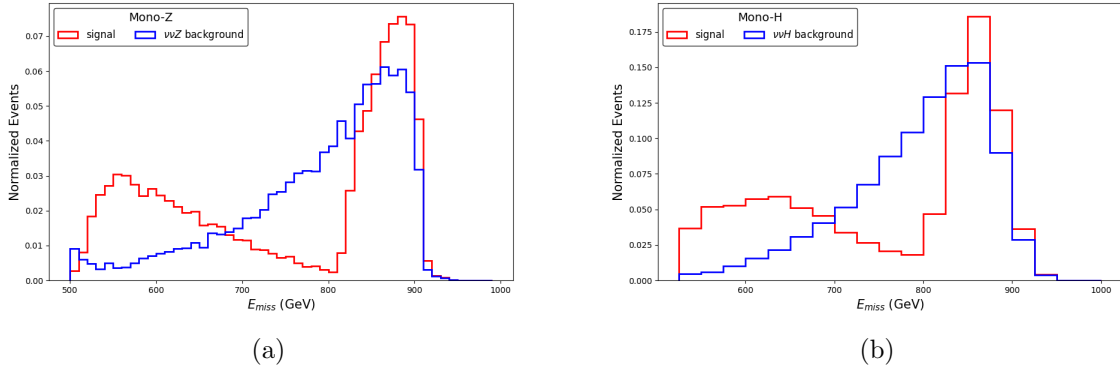


Fig. 5.6 Signal together with background. Normalized \cancel{E} distributions from operates: (a) Mono-Z: \mathcal{O}_3^s (100 GeV) and \mathcal{O}_1^f (400 GeV) (b) Mono-H: \mathcal{O}_2^s (100 GeV) and \mathcal{O}_1^s (400 GeV). We choose $\Lambda = 1.2\text{TeV}$, $\sqrt{s} = 1\text{ TeV}$ with $(P_e^+, P_e^-) : (+30\%, +80\%)$

It is clear from figure 5.5 and 5.6 that the second peak corresponding to the signal is hidden beneath the background of type $\nu\nu X$ in the signal plus background \cancel{E} distribution. To make the two peak behavior visible or noticeable even in the presence of a large irreducible background we introduce a new observable here. That is the signal significance or "local significance" S/\sqrt{B} for an integrated luminosity \mathcal{L} in \cancel{E} distribution. [30] [28]

5.3.3 Signal significance

The signal significance is defined as follows: [30]

$$\mathcal{S} = \sqrt{\left[(S + B) \log \left(1 + \frac{S}{B} \right) - S \right]} \quad (5.3)$$

Where, B and S are the background and signal events. In the limit when the background contributes ¹ more than the signal ($S/B \ll 1$), equation (5.3) can be approximated to, $\mathcal{S} = S/\sqrt{B}$ giving us the local significance. We also define the signal-to-background ratio observable, S/B , and demand a large value to ensure a two-peak behavior. Assuming we get a two-peak behavior in the bin by bin local significance plot. Let us define a few parameters that could comment distinguishability of the two peaks in a mono-X signal.

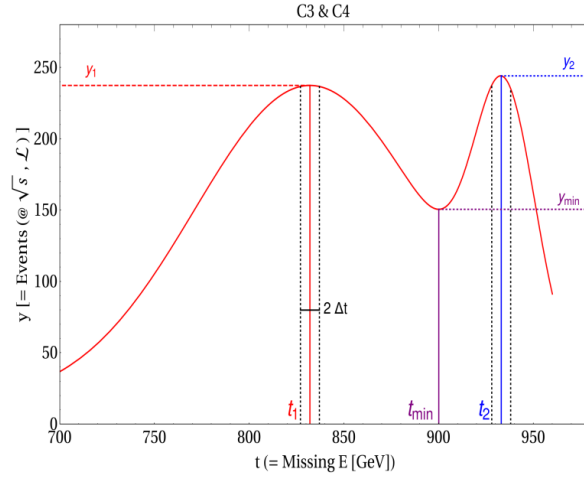


Fig. 5.7 $t \equiv \cancel{E}$ distribution with $y \equiv d\sigma/d\cancel{E}$ quantifying C3 and C4 parameters. The image is taken from paper [30]

In the figure 5.7, t_1 and t_2 denote the first and second peak position respectively. The counts at those peaks are represented by $y_1 = y_1(t_1)$ and $y_2 = y_2(t_2)$ respectively; these values correspond to the area under the curve within a small interval δt around each peak. The minima between the two peaks is labeled as t_{min} , and the event rate at this point is denoted by y_{min} . Let us now define two of these distinction criteria C3 and C4, leading to parameters R_{C_3} and R_{C_4} . [30]

- **C3:** This condition leads to the parameter R_{C_3} and it checks the significance of the second peak by comparing the number of events within a small interval of Δt around those peaks. It is defined as follows:

¹Cross section: $\sigma_B \gg \sigma_S$

$$R_{C_3} = \frac{\int_{t_1-\Delta t}^{t_1+\Delta t} y dt - \int_{t_2-\Delta t}^{t_2+\Delta t} y dt}{\int_{t_1-\Delta t}^{t_1+\Delta t} y dt + \int_{t_2-\Delta t}^{t_2+\Delta t} y dt} \quad (5.4)$$

As $\Delta t \rightarrow 0$, this simplifies to:

$$\lim_{\Delta t \rightarrow 0} R_{C_3} = \frac{y_1 - y_2}{y_1 + y_2} \quad (5.5)$$

The parameter R_{C_3} determines the number of events about the two peaks. A smaller value of R_{C_3} indicates that the second peak is more significant relative to the first one.

- **C4:** This condition leads to the parameter R_{C_4} and it checks the presence of the peaks concerning the minimum y_{\min} in between. It is defined as follows:

$$RC4 = \frac{y(t) - y(t_{\min})}{\sqrt{y(t_{\min})}} = \frac{y(t) - y_{\min}}{\sqrt{y_{\min}}} \quad (5.6)$$

Where, $t = t_2$ if $y(t_2) < y(t_1)$ and $t = t_1$ if otherwise. A large value of R_{C_4} indicates that the distinguishability of the peaks.

It is interesting to note that the cross-section corresponding to the operators showing two peak behaviors stays constant in the low mass regime and falls drastically in the high mass regime 5.8. We now select a few benchmark points and showcase the bin by bin local significance in \cancel{E} distributions and calculate the parameters described above.

Mono-X	Operators	$\{m_{\text{DM1}}, m_{\text{DM2}}\}$ (GeV)	$(\sigma_{\text{DM1}}, \sigma_{\text{DM2}})$ (fb)	L (fb $^{-1}$)	S/\sqrt{B}	RC3	RC4
γ	$(\mathcal{O}_3^f, \mathcal{O}_2^f)$	{100, 200}	(2.41, 3.19)	100	2.24 σ	30.75	0.47
γ	$(\mathcal{O}_3^f, \mathcal{O}_2^f)$	{100, 400}	(2.41, 0.54)	100	1.18 σ	77.49	0.24
Z	$(\mathcal{O}_3^s, \mathcal{O}_1^f)$	{100, 400}	(0.15, 0.14)	1000	1.92 σ	14.21	3.42
H	$(\mathcal{O}_2^s, \mathcal{O}_1^s)$	{100, 400}	(0.09, 0.10)	1000	0.8 σ	14	1.59

Table 5.2 Benchmark points in Mono-X

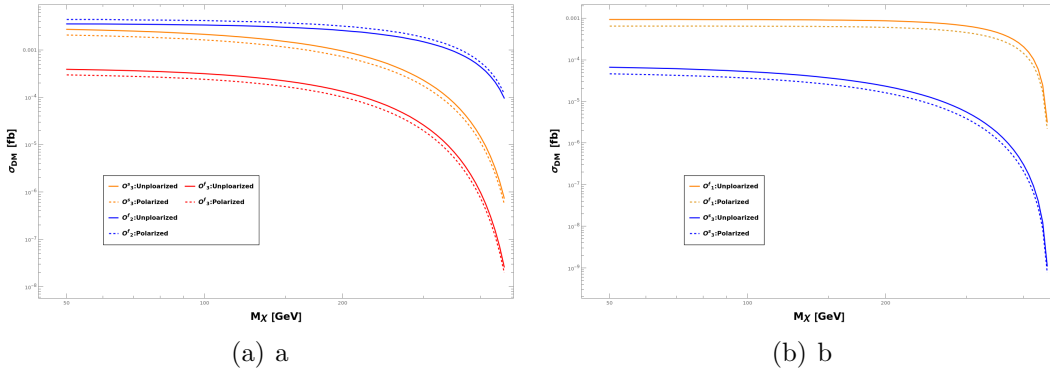


Fig. 5.8 (a) Cross-section variation with DM mass for operators giving the mono-Z signal. (b) Cross-section variation with DM mass for operators giving the mono- γ signal. For both the cases, $\sqrt{s} = 1 \text{ TeV}$, $C_{DM} = 1$, $\Lambda = 1200 \text{ GeV}$ and Polarization: $(P_e^+, P_e^-) = (30\%, 80\%)$ is set.

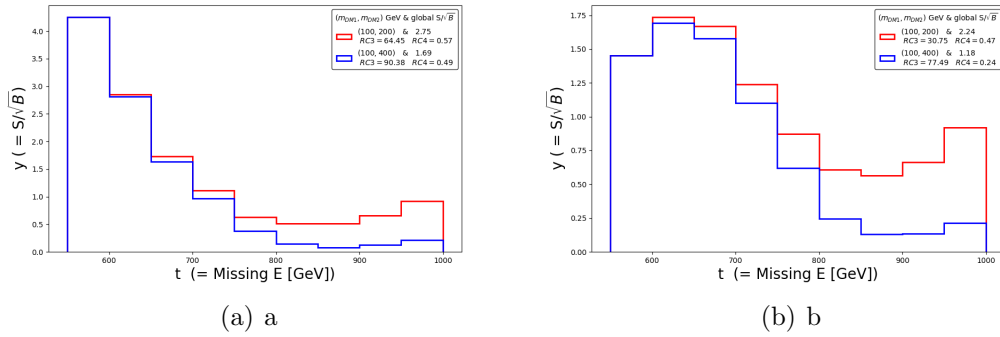


Fig. 5.9 (a) Variation of signal significance in \cancel{E} distribution for operators $(\mathcal{O}_3^s, \mathcal{O}_2^f)$ for two sets of DM mass. (b) Variation of signal significance in \cancel{E} distribution for operators $(\mathcal{O}_3^f, \mathcal{O}_2^s)$ for two sets of DM mass. For both the cases, $\sqrt{s} = 1 \text{ TeV}$, $(C_{DM1}, C_{DM2}) = (1.5, 1)$, $\Lambda = 1200 \text{ GeV}$ and Polarization: $(P_e^+, P_e^-) = (30\%, 80\%)$ is set.

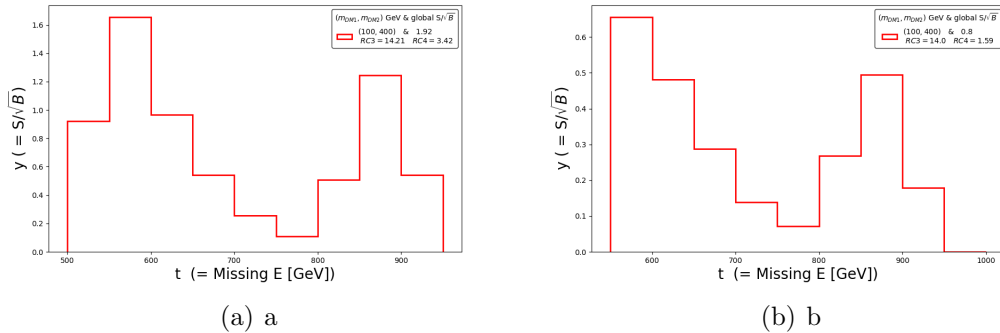


Fig. 5.10 (a) Variation of signal significance in \cancel{E} distribution for operators $(\mathcal{O}_3^s, \mathcal{O}_1^f)$: Mono-Z $(C_{DM1}, C_{DM2}) = (2, 1)$. (b) Variation of signal significance in \cancel{E} distribution for operators $(\mathcal{O}_2^s, \mathcal{O}_1^s)$: Mono-H $(C_{DM1}, C_{DM2}) = (1, 1)$. For both the cases, $\sqrt{s} = 1 \text{ TeV}$, $\Lambda = 1200 \text{ GeV}$ and Polarization: $(P_e^+, P_e^-) = (30\%, 80\%)$ is set.

Figure 5.9 and 5.10 show the variation of local significance for two sets of operators showing the two peak behavior. It is worth noting that for a higher value of \mathcal{O}_f^2 mass, the cross-section decreases resulting in decreasing global significance and hence the distinguishability of two peaks. We get a two peak behavior in local significance for the operators of nearly the same production cross-section. The Wilson coefficients are set to the values as described keeping that in mind.

5.4 Summary and Conclusion

This work is based on the paper "*Mono-X signal and two-component dark matter*" [28]. We began this chapter by introducing the idea of a two-component DM framework. This possibility provides a rich phenomenology like coupled Boltzmann equations to determine relic contribution, interactions between DM components, large parameter space, etc. We do a model-independent study of DM and describe DM-SM effective operators 5.1. Mono-X events plus missing energy give a telltale signature of the DM pair production at colliders.

Identifying and separating two WIMP DM components at colliders is a challenging task as the main signal of both DM components is of the mono-X type ($X = \gamma, Z, H$). We study these two peak behavior in the missing energy \cancel{E} distribution arising from a set of operators giving the mono-X signal. However, the huge SM background of the type $\nu\nu X$, where missing neutrinos in the detector can mimic the presence of DM signals, gives a falsified signal hiding one peak beneath it in the \cancel{E} distribution. To make the two peak behavior visible or noticeable even in the presence of a large irreducible background we introduced bin-by-bin distributions in signal significance \sqrt{S}/B plotted against \cancel{E} to infer the presence of the second peak. We then defined parameters R_{C_3} and R_{C_4} to measure the significance of the second peak relative to the first one. [30]

The operators 5.1 are implemented as an extension of the SM Lagrangian using `FeynRules` [22] and `LanHEP` [23]. The model file is then fed to `MadGraph5` [25] to generate events. Event files are then passed to `Pythia8` [26] and `Delphes` [31] for Hadronization and Detector-level simulation respectively. The package `MicrOMEGAs` [24] is used to calculate Dark Matter properties.

Chapter 6

Future Prospects

6.1 Revisiting Two component DM framework

The previous analysis used arbitrary EFT parameters. However, it's essential to consider the current experimental limits derived from Indirect and Direct searches, along with constraints from relic abundance, to ensure the validity of the analysis. The DM relic density value from the CMB measurements provides the most stringent bound for the EFT parameters, Λ , C , and mass of the DM, m_{DM} . In a two-component DM setup, both DM components stemming from two different operators are produced under abundance, such that their combination matches the observed relic abundance. The measured value of the relic density obtained from Planck data is, [12]

$$\Omega_{DM}h^2 = \Omega_{DM1}h^2 + \Omega_{DM2}h^2 = 0.11933 \pm 0.00091 \quad (6.1)$$

6.2 Relic Constraint

We start this exercise with two operators, namely, \mathcal{O}_3^s , \mathcal{O}_1^f 5.1 which give rise to the Mono-Z signal. The EFT-free parameters are $(m_{DM1}, C1, \Lambda)$ and $(m_{DM2}, C2, \Lambda)$. We keep $\Lambda = 1.2$ TeV fixed in our analysis and constraint $(m_{DM1}, C1)$ and $(m_{DM2}, C2)$ plane.

- \mathcal{O}_f^1 : The dimension 6 operator gives rise to $2_{DM} \rightarrow 2_{SM}$ annihilation processes. The following Feynman diagrams contribute to the freeze-out of DM particle χ . Below, l indicates SM leptons (e, μ, τ), and ν_l indicates SM neutrinos (ν_e, ν_μ, ν_τ)

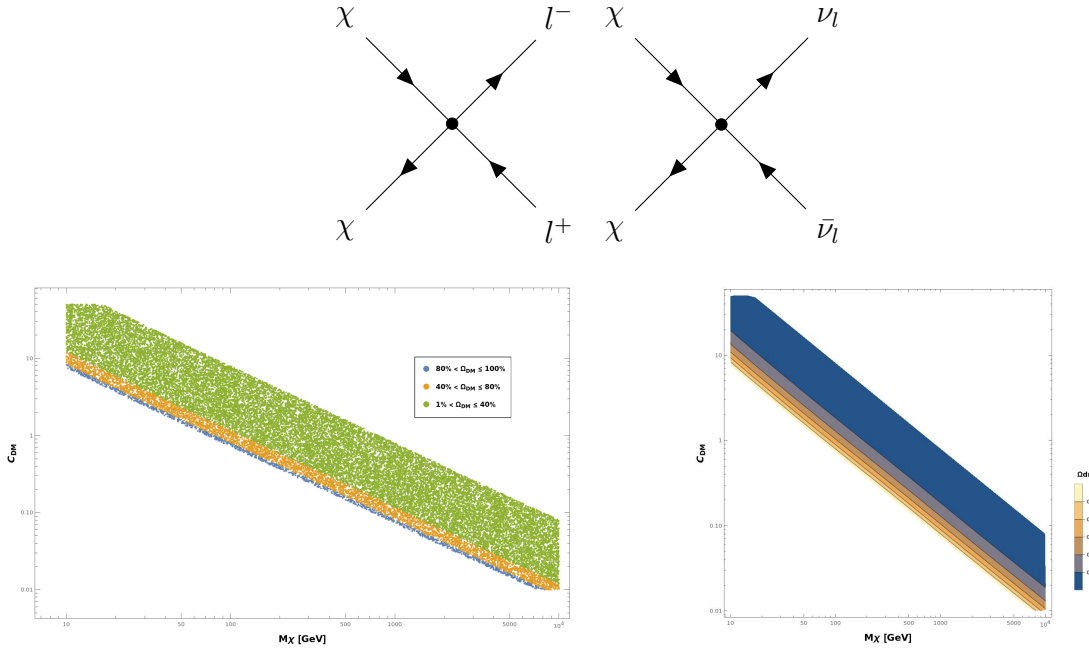


Fig. 6.1 Relic density allowed parameter space in $m_{dm1} - C_{dm1}$ plane. Different colors indicate the percentage of relic density. New Physics scale, $\Lambda = 1200$ GeV is set.

- \mathcal{O}_s^3 : The dimension 6 operator gives rise to $2_{DM} \rightarrow 2_{SM}$ annihilation processes. The following Feynman diagrams contribute to the freeze-out mechanism,

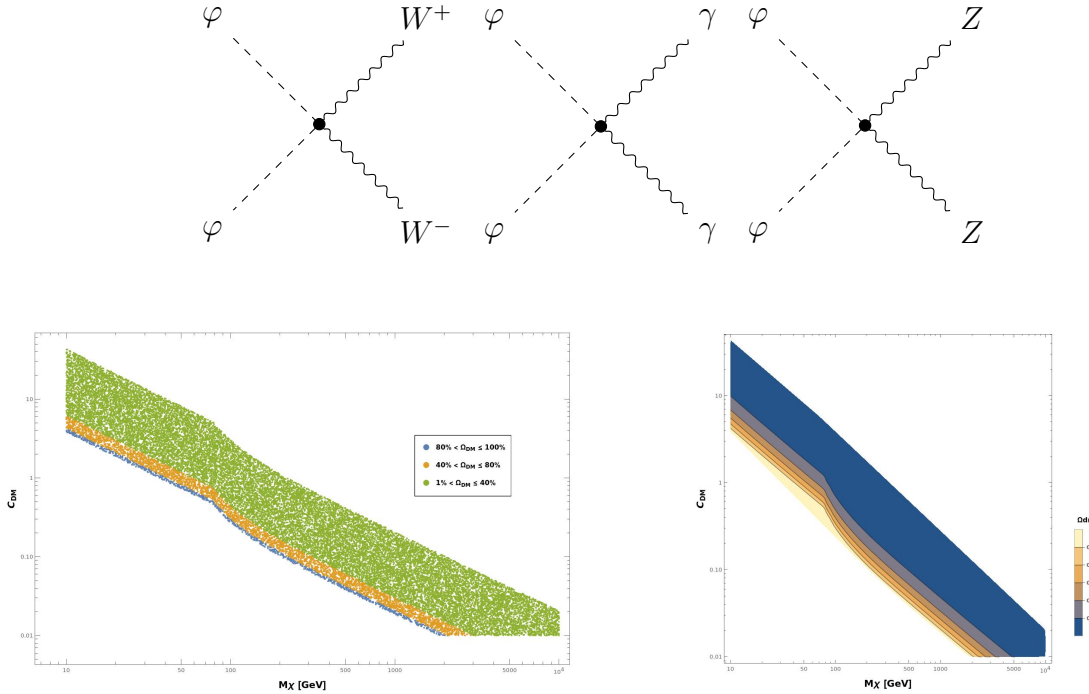


Fig. 6.2 Relic density allowed parameter space in $m_{dm2} - C_{dm2}$ plane. Different colors indicate the percentage of relic density. New Physics scale, $\Lambda = 1200$ GeV is set.

We observe from the above plots that as the DM mass is increased, the Wilson coefficient or coupling decreases to satisfy the relic density constraints as the relic density of thermal WIMPs is given by, $\Omega_{DM}h^2 \approx 1/\langle\sigma V\rangle \approx 1/C^2m_{DM}^2$ (for a fixed value of Λ). We are now interested in constraining the $(m_{DM1} - C_{DM1})$ and $(m_{DM2} - C_{DM2})$ plane for a combination of under-abundant relics from \mathcal{O}_1^f and \mathcal{O}_3^s respectively, ensuring that their sum satisfies the observed relic abundance. (6.1)

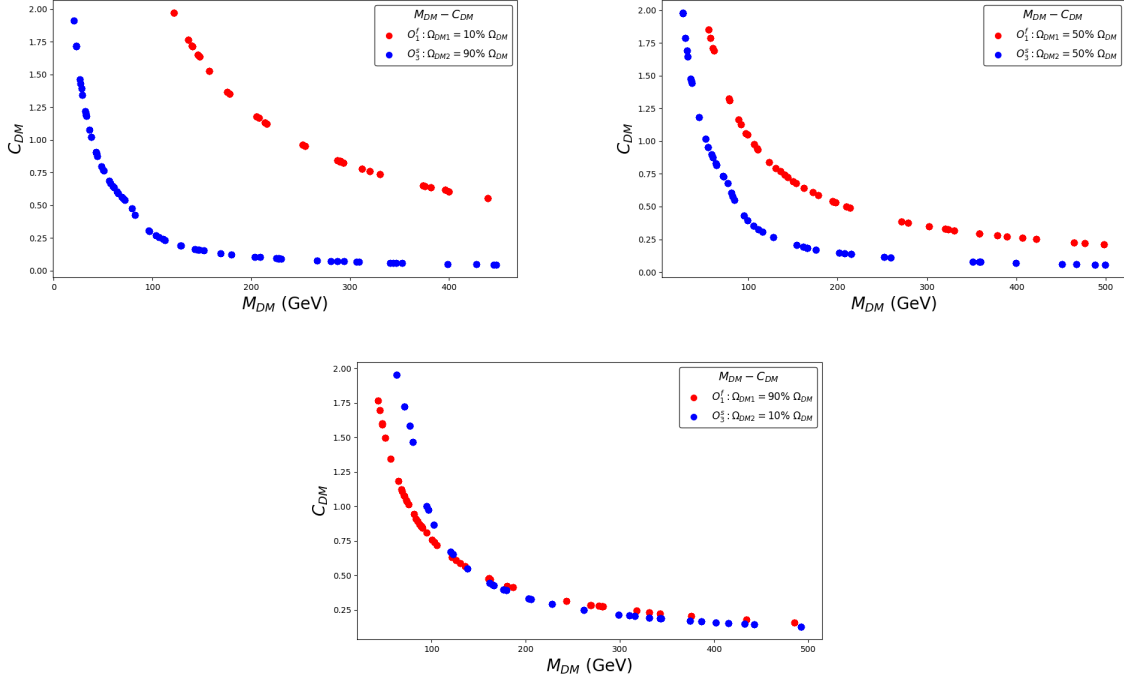


Fig. 6.3 Left: $(\mathcal{O}_1^f, \mathcal{O}_3^s) = (10\%, 90\%)$ Middle: $(\mathcal{O}_1^f, \mathcal{O}_3^s) = (50\%, 50\%)$ Right: $(\mathcal{O}_1^f, \mathcal{O}_3^s) = (90\%, 10\%)$; contribution $C_{DM}M_{DM}$ plane

The figure 6.3 indicates the allowed values of (C_{DM1}, M_{DM1}) for under abundance \mathcal{O}_1^f and (C_{DM2}, M_{DM2}) for under abundance \mathcal{O}_3^s such that the total satisfies the observed relic. The aim is to select benchmark points for different combinations and determine which parameters offer the best distinguishability of the two peaks in the bin-by-bin local significance distribution in the \mathcal{E} distribution.

6.3 Conclusion

In a two-component DM setup, both DM components stemming from two different operators are produced under abundance, such that their combination matches the observed relic abundance. With this objective in mind, we impose constraints on the (C_{DM}, m_{DM}) plane for both DM components. Our future goal is to identify

benchmark points representing different combinations of these parameters. By doing so, we seek to determine which parameter space enables the most effective differentiation between the two peaks observed in the local significance against the \cancel{E} distribution. Additionally, the parameter space can be further constrained by Direct and Indirect searches. This exploration will be pursued in the future to refine the parameter space for DM searches at the International Linear Collider. [21]

Chapter 7

Appendix

7.1 The Boltzmann Equation

The Boltzmann equation describes the time evolution of the number density of a particular species that is not in a state of thermal equilibrium. Here, we are interested in looking for dark matter relic density as it decoupled from the visible sector particles. We look at the phase space evolution of the distribution function, $f(p^\mu, x^\mu)$ given by the Boltzmann equation of the form, [9] [11]

$$\hat{\mathbf{L}}[f] = \mathbf{C}[f] \quad (7.1)$$

Where \mathbf{C} is the collision operator and $\hat{\mathbf{L}}$ is the Liouville operator.

The non-relativistic Liouville operator which gives the total time derivative of the phase space density, $f(\mathbf{p}, \mathbf{x})$ of a particle species of mass m and experiencing an external force \mathbf{F} is given by,

$$\begin{aligned} \mathbf{L}_{\text{NR}} &= \frac{\partial}{\partial t} + \frac{dx}{dt} \cdot \vec{\nabla}_x + \frac{dp}{dt} \cdot \vec{\nabla}_p \\ &= \frac{\partial}{\partial t} + \vec{v} \cdot \vec{\nabla}_x + \vec{F} \cdot \vec{\nabla}_p \end{aligned} \quad (7.2)$$

The relativistic covariant form the Liouville operator is given by,

$$\hat{\mathbf{L}} = p^\alpha \frac{\partial}{\partial x^\alpha} + \frac{dp^\alpha}{d\tau} \frac{\partial}{\partial p^\alpha} \quad (7.3)$$

Where, p is the four momentum and τ is the proper time. Time evolution of particles is along the geodesic when collision term is not considered. A curve

resulting from parallel transporting a vector along itself describes a geodesic. Consider a vector $\frac{d}{d\tau}$,

$$\begin{aligned}
 \nabla_{\frac{d}{d\tau}}\left(\frac{d}{d\tau}\right) &= 0 \\
 \therefore \frac{d}{d\tau}\left(\frac{d}{d\tau}\right) &= 0 \\
 \therefore \frac{d}{d\tau}\left(\frac{dx^\alpha}{d\tau}\frac{d}{dx^\alpha}\right) &= 0 \\
 \therefore \frac{d^2x^\alpha}{d\tau^2}\frac{\partial}{\partial x^\alpha} + \frac{dx^\alpha}{d\tau}\frac{d}{d\tau}\left(\frac{\partial}{\partial x^\alpha}\right) &= 0 \\
 \therefore \frac{d^2x^\alpha}{d\tau^2}\frac{\partial}{\partial x^\alpha} + \frac{dx^\alpha}{d\tau}\left(\frac{dx^\beta}{d\tau}\frac{\partial}{\partial x^\beta}\left(\frac{\partial}{\partial x^\alpha}\right)\right) &= 0 \\
 \therefore \frac{dv^\alpha}{d\tau}\frac{\partial}{\partial x^\alpha} + v^\alpha v^\beta \Gamma_{\alpha\beta}^k e_k &= 0
 \end{aligned} \tag{7.4}$$

Where, $\frac{\partial}{\partial x^k} = e_k$ (Basis vector;)

$\frac{\partial e^\alpha}{dx^\beta} = \Gamma_{\alpha\beta}^k e_k$ (Christoffel symbol)

$$\left(\frac{dv^k}{d\tau} + v^\alpha v^\beta \Gamma_{\alpha\beta}^k\right)e_k = 0 \tag{7.5}$$

$$\left(\frac{dp^k}{d\tau} + p^\alpha p^\beta \Gamma_{\alpha\beta}^k\right)e_k = 0$$

Using the above equation, we can look back at equation 1.5 and write it as follows,

$$\hat{\mathbf{L}} = p^\alpha \frac{\partial}{\partial x^\alpha} - p^\gamma p^\beta \Gamma_{\beta\gamma}^\alpha \frac{\partial}{\partial p^\alpha} \tag{7.6}$$

We are interested in writing the Liouville operator for the Friedmann-Robertson-Walker (FRW) model of the universe which is spatially homogeneous and isotropic. Looking at this we can figure out that the phase space density is now independent of position parameter; $f(p^\alpha, t)$.

We can further look at equation 1.8 and figure out that as f doesn't evolve with x , $\alpha = 0$ thus the phase space density can be described by, $f(E, t)$.

$$\hat{\mathbf{L}}[f] = E \frac{\partial f}{\partial t} - p^\gamma p^\beta \Gamma_{\beta\gamma}^0 \frac{\partial f}{\partial E} \quad (7.7)$$

The FRW metric is given by,

$$g_{ij} = \begin{bmatrix} -1 & 0 & 0 & 0 \\ 0 & a(t)^2 & 0 & 0 \\ 0 & 0 & a(t)^2 & 0 \\ 0 & 0 & 0 & a(t)^2 \end{bmatrix} \quad (7.8)$$

Where, $a(t)$ is a scale factor.

Calculating Christoffel symbols for the above metric gives us,

$$\begin{aligned} \Gamma_{\beta\gamma}^0 &= a(t)\dot{a}(t) \quad \forall \quad \beta = \gamma \\ \Gamma_{\beta\gamma}^0 &= 0 \quad \forall \quad \beta \neq \gamma \end{aligned} \quad (7.9)$$

From the above we can write the Liouville operator as follows,

$$\hat{\mathbf{L}}[f] = E \frac{\partial f}{\partial t} - \frac{\dot{a}(t)}{a(t)} |\vec{p}|^2 \frac{\partial f}{\partial E} \quad (7.10)$$

Where, $\frac{\dot{a}(t)}{a}$ is the Hubble constant, H .

To get number density, we integrate phase space density over the momenta space,

$$n = \frac{g}{(2\pi)^3} \int d^3p f(E, t) \quad (7.11)$$

Where, g is D.O.F of a particle species.

As we are integrating over momenta space we would like to make following changes to Liouville operator,

According to the energy-momentum relation,

$$\begin{aligned}
 E &= \sqrt{p^2 + m^2} \\
 dE &= \frac{|p|d|p|}{E} \\
 \frac{\partial}{\partial E} &= \frac{d|p|}{dE} \frac{\partial}{\partial |p|} \\
 \frac{\partial}{\partial E} &= \frac{E}{|p|} \frac{\partial}{\partial |p|}
 \end{aligned} \tag{7.12}$$

From the above equations and equation (1.3) we can write,

$$\frac{\partial f}{\partial t} - H|\vec{p}| \frac{\partial f}{\partial p} = \frac{\mathbf{C}[f]}{E} \tag{7.13}$$

We're interested in calculating time evolution of number density, therefore,

$$\begin{aligned}
 \frac{dn}{dt} &= \frac{g}{(2\pi)^3} \int d^3p \frac{\partial f}{\partial t} \\
 \frac{dn}{dt} &= \frac{g}{(2\pi)^3} \int d^3p (H|\vec{p}| \frac{\partial f}{\partial p} + \frac{\mathbf{C}[f]}{E})
 \end{aligned} \tag{7.14}$$

In spherical co-ordinates in momenta space, $d^3p = 4\pi|\vec{p}|^2 dp$

$$\begin{aligned}
 \frac{dn}{dt} &= \frac{g}{(2\pi)^3} 4\pi H \int dp |p|^3 \frac{\partial f}{\partial |p|} + \frac{g}{(2\pi)^3} \int d^3p \frac{\mathbf{C}[f]}{E} \\
 \frac{dn}{dt} &= \frac{g}{(2\pi)^3} 4\pi H ([|p|^3 f]|_0^\infty - \int 3|p|^2 f dp) + \frac{g}{(2\pi)^3} \int d^3p \frac{\mathbf{C}[f]}{E}
 \end{aligned} \tag{7.15}$$

As f goes to zero at $p = \infty$ the boundary term vanishes.

$$\frac{dn}{dt} = -3 \frac{g}{(2\pi)^3} H \int d^3p f + \frac{g}{(2\pi)^3} \int d^3p \frac{\mathbf{C}[f]}{E} \tag{7.16}$$

From equation 1.13,

$$\boxed{\frac{dn}{dt} + 3Hn = \frac{g}{(2\pi)^3} \int d^3p \frac{\mathbf{C}[f]}{E}} \tag{7.17}$$

We can see that even when there is no interaction among the species, the number density evolves due to the Hubble expansion constant. To scale out the effect of

expansion of the Universe we make the following transformation, $Y \equiv \frac{n}{s}$, where, s is the entropy density.

Using conservation of entropy,
 $entropy = (sa)^3 = constant$

$$\begin{aligned}\frac{d}{dt}(sa^3) &= 0 \\ \dot{s} + 3\frac{\dot{a}}{a}s &= 0 \\ \dot{s} + 3Hs &= 0\end{aligned}\tag{7.18}$$

Using above equation,

$$\begin{aligned}\frac{dn}{dt} &= \frac{d}{dt}(Ys) \\ &= s\frac{dY}{dt} + Y\dot{s} \\ &= s\frac{dY}{dt} - 3Hn\end{aligned}\tag{7.19}$$

Substituting above equation in (1.19),

$$\boxed{s\frac{dY}{dt} = \frac{g}{(2\pi)^3} \int d^3|p| \frac{\mathbf{C}[f]}{E}}\tag{7.20}$$

The collision term takes different forms for different models in study. Here one such model is showed.

7.2 The WIMP case

Consider the generic two to two annihilation and creation processes,

$$1 + 2 \longleftrightarrow 3 + 4$$

We need to evaluate the right hand side of equation (2.22) for the given process. It is given by,

$$\begin{aligned} \frac{g}{(2\pi)^3} \int d^3|p| \frac{\mathbf{C}[f_1]}{E} = - \int d\pi_1 d\pi_2 d\pi_3 d\pi_4 (2\pi)^4 \delta^4(p_1 + p_2 - p_3 - p_4) \\ [|M|_{1+2 \rightarrow 3+4}^2 f_1 f_2 (1 \pm f_3)(1 \pm f_4) - |M|_{3+4 \rightarrow 1+2}^2 f_3 f_4 (1 \pm f_1)(1 \pm f_2)] \end{aligned} \quad (7.21)$$

Where, (+) applies to bosons; (—) applies to fermions and,

$$d\pi_i = \frac{g_i}{(2\pi)^3} \frac{d^3 p}{2E}$$

There are two well motivated assumptions that greatly simplify equation (2.23)

- 1) T invariance or CP invariance : $|M|_{1+2 \rightarrow 3+4}^2 = |M|_{3+4 \rightarrow 1+2}^2 = |M|^2$
- 2) Approximating to Maxwell Boltzmann statistics for all species instead of using Fermi-Dirac for fermions and Bose Einstein for bosons. This removes the blocking, $1 \pm f_i \approx 1$

Using these approximations, we get,

$$\frac{g}{(2\pi)^3} \int d^3|p| \frac{\mathbf{C}[f_1]}{E} = - \int d\pi_1 d\pi_2 d\pi_3 d\pi_4 (2\pi)^4 \delta^4(p_1 + p_2 - p_3 - p_4) |M|^2 [f_1 f_2 - f_3 f_4] \quad (7.22)$$

Now, let's consider that product particles i.e. species 3 and 4 remains in thermal equilibrium. MB statistics gives,

$$f_3 = e^{-\frac{E_3}{T}} \text{ and } f_4 = e^{-\frac{E_4}{T}}$$

The 0^{th} component the mass shell term of equation (2.23), will impose the energy conservation i.e.,

$$E_1 + E_2 = E_3 + E_4$$

$$\therefore f_3 f_4 = e^{-\frac{E_3 + E_4}{T}} = e^{-\frac{E_1 + E_2}{T}} = f_1^{eq} f_2^{eq}$$

Substituting the above result in equation (2.24), we get,

$$\frac{g}{(2\pi)^3} \int d^3|p| \frac{\mathbf{C}[f_1]}{E} = - \int d\pi_1 d\pi_2 d\pi_3 d\pi_4 (2\pi)^4 \delta^4(p_1 + p_2 - p_3 - p_4) |M|^2 [f_1 f_2 - f_1^{eq} f_2^{eq}] \quad (7.23)$$

$$\frac{g}{(2\pi)^3} \int d^3|p| \frac{\mathbf{C}[f_1]}{E} = - \int d\pi_1 d\pi_2 d\pi_3 d\pi_4 (2\pi)^4 \delta^4(p_1 + p_2 - p_3 - p_4) |M|^2 f_1^{eq} f_2^{eq} \left[\frac{f_1 f_2}{f_1^{eq} f_2^{eq}} - 1 \right] \quad (7.24)$$

Now, the interaction term can be written in terms of n_i , the actual number density of species, i , and n_i^{eq} , the equilibrium number density of species, i ,

$$\frac{f_i}{f_i^{eq}} = \frac{n_i}{n_i^{eq}}$$

$$\frac{g}{(2\pi)^3} \int d^3|p| \frac{\mathbf{C}[f_1]}{E} = - \int d\pi_1 d\pi_2 d\pi_3 d\pi_4 (2\pi)^4 \delta^4(p_1 + p_2 - p_3 - p_4) |M|^2 f_1^{eq} f_2^{eq} \left[\frac{n_1 n_2}{n_1^{eq} n_2^{eq}} - 1 \right] \quad (7.25)$$

$$\frac{g}{(2\pi)^3} \int d^3|p| \frac{\mathbf{C}[f_1]}{E} = - \frac{1}{n_1^{eq} n_2^{eq}} \int d\pi_1 d\pi_2 d\pi_3 d\pi_4 (2\pi)^4 \delta^4(p_1 + p_2 - p_3 - p_4) |M|^2 f_1^{eq} f_2^{eq} [n_1 n_2 - n_1^{eq} n_2^{eq}] \quad (7.26)$$

$$\therefore \frac{g}{(2\pi)^3} \int d^3|p| \frac{\mathbf{C}[f_1]}{E} = - \langle \sigma_{1+2 \rightarrow 3+4} |v| \rangle [n_1 n_2 - n_1^{eq} n_2^{eq}] \quad (7.27)$$

Where, the thermally-averaged annihilation cross section times velocity, $\langle \sigma_{1+2 \rightarrow 3+4} |v| \rangle$ is defined as,

$$\langle \sigma_{1+2 \rightarrow 3+4} |v| \rangle = \frac{1}{n_1^{eq} n_2^{eq}} \int d\pi_1 d\pi_2 d\pi_3 d\pi_4 (2\pi)^4 \delta^4(p_1 + p_2 - p_3 - p_4) |M|^2 f_1^{eq} f_2^{eq} \quad (7.28)$$

Substituting expression from equation (2.30) into equation (2.22),

$$s \frac{dY_1}{dt} = - \langle \sigma_{1+2 \rightarrow 3+4} |v| \rangle [n_1 n_2 - n_1^{eq} n_2^{eq}] \quad (7.29)$$

Substituting, $n_1 = Y_1 s$,

$$\frac{dY_1}{dt} = - \langle \sigma_{1+2 \rightarrow 3+4} |v| \rangle s [Y_1 Y_2 - Y_1^{eq} Y_2^{eq}] \quad (7.30)$$

As, the interaction term usually depends explicitly on the temperature, we will define a new variable, $x \equiv \frac{m}{T}$, where m is the mass of particle and T is the temperature.

During the radiation-dominated era, x and t are related by,

$$\begin{aligned} t &= \frac{0.301}{\sqrt{g_*}} \frac{m_{pl}}{T^2} \\ &= \frac{1}{2} \frac{x^2}{1.66\sqrt{g_*}} \frac{m_{pl}}{m^2} \\ &= \frac{x^2}{2H(m)} \end{aligned} \quad (7.31)$$

Where, g_* is the effectively massless degrees of freedom, $m_{pl} = 1.22 \times 10^{19}$ GeV is the Planck Mass and $H(m)$ is defined as, $H(m) \equiv \frac{1.66\sqrt{g_*}m^2}{m_{pl}}$

$$\therefore dt = \frac{x dx}{H(m)} \quad (7.32)$$

Substituting the above expression into equation (2.32), we get,

$$\frac{dY_1}{dt} \frac{H(m)}{x} = -\langle \sigma_{1+2 \rightarrow 3+4} | v | \rangle s [Y_1 Y_2 - Y_1^{eq} Y_2^{eq}] \quad (7.33)$$

$$\therefore \frac{dY_1}{dt} = -\frac{x s}{H(m)} \langle \sigma_{1+2 \rightarrow 3+4} | v | \rangle [Y_1 Y_2 - Y_1^{eq} Y_2^{eq}] \quad (7.34)$$

Defining the temperature independent parameters as, $s_0 = s x^3$ and $\sigma_0 = \langle \sigma_{1+2 \rightarrow 3+4} | v | \rangle x^n$

Substituting these parameters into equation (2.36),

$$\therefore \frac{dY_1}{dt} = -\frac{x s_0 \sigma_0}{H(m) x^{n+3}} [Y_1 Y_2 - Y_1^{eq} Y_2^{eq}] \quad (7.35)$$

$$\therefore \frac{dY_1}{dt} = -\frac{\lambda}{x^{n+2}} [Y_1 Y_2 - Y_1^{eq} Y_2^{eq}] \quad (7.36)$$

Defining, m_{DM} as the mass of dark matter particle,

$$\begin{aligned} s_0 &= \frac{2\pi^2}{45} g_{*s} m_{DM}^3 \\ H(m_{DM}) &= \frac{1.66\sqrt{g_*} m_{DM}^2}{m_{pl}} \\ \therefore \lambda &\equiv \frac{s_0 \sigma_0}{H(m_{DM})} = 0.264 \frac{g_{*s}}{\sqrt{g_*}} m_{pl} m_{DM} \sigma_0 \end{aligned}$$

Let us consider an annihilation process of type, $2_{DM} \rightarrow 2_{SM}$

$$\begin{aligned}\chi_{DM} + \bar{\chi}_{DM} &\rightarrow \psi_{SM} + \bar{\psi}_{SM} \\ \therefore Y_1 &= Y_\chi, Y_2 = Y_{\bar{\chi}}\end{aligned}$$

Assuming the matter-antimatter asymmetry, $Y Y_\chi = Y_{\bar{\chi}} = Y$
Substituting the above results into equation (2.38) we get,

$$\therefore \boxed{\frac{dY}{dt} = -\frac{\lambda}{x^{n+2}}[Y^2 - (Y^{eq})^2]} \quad (7.37)$$

In the relativistic ($x \ll 3$) case resulting into Hot Relic and the non-relativistic case ($x \gg 3$) resulting into Cold Relic, the equilibrium value of the number of χ 's per co-moving volume takes the form,

$$\begin{aligned}Y^{eq}(x) &= 0.278 \frac{g_{eff}}{g_{*s}} \quad (x \ll 3) \\ Y^{eq}(x) &= 0.145 \frac{g}{g_{*s}} x^{3/2} e^{-x} \quad (x \gg 3)\end{aligned} \quad (7.38)$$

Where, $g_{eff} = g$ for bosons and $g_{eff} = 3g/4$ for fermions. [11] [9] [10]

7.3 Introduction to Collider Physics

For several decades, high-energy accelerators and colliders have served as our primary tools for discovering new particles and testing fundamental interactions. The groundbreaking discovery of the Higgs boson at the Large Hadron Collider (LHC) in July 2012 marked a significant milestone in the history of physics. With ongoing preparations for the International Linear Collider (ILC), there is a growing anticipation that we're on the verge of exploring physics Beyond the Standard Model. In this section, we discuss collider parameters, Kinematics, and observables, followed by a brief discussion about techniques used to simulate collider events. [32] [33]

7.3.1 Overview

- **C.O.M Energy:** In a collision of two particles of masses m_1 and m_2 with four-momentum, $p_1^\mu = (E_1, \vec{p}_1)$ and $p_2^\mu = (E_2, \vec{p}_2)$, we define Lorentz invariant Mandelstam variable:

$$s \equiv (p_1^\mu + p_2^\mu)^2 = \begin{cases} (E_1 + E_2)^2 & \text{C.O.M. Frame } \vec{p}_1 + \vec{p}_2 = 0 \\ m_1^2 + m_2^2 + 2(E_1 E_2 - \vec{p}_1 \cdot \vec{p}_2) & \end{cases} \quad (7.39)$$

where, $p^\mu p_\mu = E^2 - \vec{p} \cdot \vec{p} = m^2$. In the context of High Energy Colliders, the beam particles are highly relativistic, therefore their masses can be ignored. We define the total center of mass energy E_{CM} as \sqrt{s} :

$$E_{CM} \equiv \sqrt{s} = \begin{cases} 2E & E_1 \approx E_2 \text{ C.O.M. Frame} \\ \sqrt{2E_2 m_1} & \text{Fixed target with } \vec{p}_1 = 0 \end{cases} \quad (7.40)$$

- **Cross-Section:** AT colliders, collisions occur between beams comprising a large number of particles. When two beams collide head-on, the number of scattered particles is expected to be proportional to the number of particles in each beam, denoted as N_1 and N_2 , respectively, and inversely proportional to the cross-sectional area, a . The proportionality constant is defined as the scattering cross-section for the given final state.

$$\sigma = \frac{(\text{Number of scattered events}) \cdot a}{N_1 \cdot N_2} \quad (7.41)$$

It is clear from the expression that the cross-section has a unit of cm^2 in cgs. In particle physics, we define *Barn* as a unit of cross-section. Where, $1barn = 10^{-24}cm^2$

- **Luminosity:** If the beams collide at a frequency of f , the recorded number of scattered particles, N can be written as,

$$N = \mathcal{L}\sigma \quad (7.42)$$

Where

$$\mathcal{L} = \frac{fN_1N_2}{a}$$

Where, σ is the production cross section and \mathcal{L} is the instantaneous luminosity. \mathcal{L} has a unit of $cm^{-2}s^{-1}$ or $b^{-1}s^{-1}$

- **Synchrotron Radiation:** Charged particles in circular colliders can emit electromagnetic radiation known as synchrotron radiation.

$$\Delta E \propto \frac{1}{R} \left(\frac{E}{m_p} \right)^4 \quad (7.43)$$

Where R is the radius of the circular collider, E is the collision energy and m_p is the mass of the colliding particle. It is clear from the above expression that for a massive particle or large radius collider, energy loss due to synchrotron radiation could be avoided. [33]

7.3.2 Collider Kinematics

At hadron colliders like the LHC, two protons collide head-on, each carrying a specific momentum. In the context of a $13;TeV$ collision at the LHC, this entails two protons traveling in opposite directions each with a momenta of $6.5;TeV$. Assuming the proton mass is negligible given the \sqrt{s} , the four-momenta of these protons are: [32]

$$\begin{aligned} P_1^\mu &= (6.5TeV, 0, 0, 6.5TeV) \\ P_2^\mu &= (6.5TeV, 0, 0, -6.5TeV) \end{aligned} \quad (7.44)$$

The partons carry only a fraction of the proton momenta. As such,

$$\begin{aligned} p_1^\mu &= x_1 P_1^\mu \\ p_2^\mu &= x_2 P_2^\mu \end{aligned} \quad (7.45)$$

The fractions x_1 and x_2 denote the momentum carried by the partons within the proton, and these fractions are probabilistic and independent. At the proposed *International Linear Collider (ILC)* [21] which collides $\mathbf{e}^+\mathbf{e}^-$ one does not need to worry about the parton distribution as the leptons are composite particles carrying all the momentum. Now, upon collision, we might be interested in the angular distribution of the colliding particles. The azimuthal angle, ϕ , is measured around the beam line. However, due to the net momenta of the colliding particles along the z -direction, the separation in their polar angle, θ , varies with the momenta in the z -direction, thus altering its value in different frames. As angles are less informative in partonic collisions, we utilize quantities that remain invariant under longitudinal boosts. Two such quantities are the transverse momenta, function of p_x and p_y . Both the scalar and vector combinations of these quantities are used. Additionally, ϕ remains invariant under longitudinal boosts.

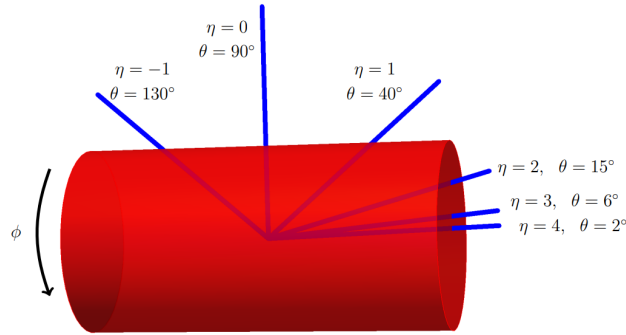


Fig. 7.1 Polar angle: θ ; Pseudorapidity η and Lorentz invariant quantity, Azimuthal angle: ϕ

$$\begin{aligned} \vec{p}_T &= (p_x, p_y) \\ p_T &= \sqrt{p_x^2 + p_y^2} \\ \phi &= \tan^{-1} \frac{p_x}{p_y} \end{aligned} \quad (7.46)$$

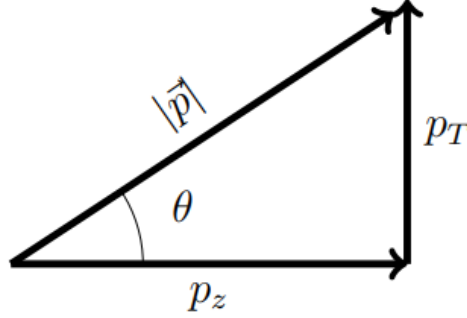
Another important quantity is rapidity, y defined as follows:

$$y = \frac{1}{2} \ln \frac{E + p_z}{E - p_z} \quad (7.47)$$

While the rapidity is not a Lorentz variant quantity, the difference in the rapidities for two momenta p_1 and p_2 is boost invariant. This motivates us to define, angular separation ΔR :

$$\Delta R = \sqrt{(\Delta\phi)^2 + (\Delta y)^2} \quad (7.48)$$

Angular separation is clearly a boost invariant quantity. For massless particles, we define yet another quantity called Pseudorapidity η :



For massless particles $E = |\vec{p}|$, therefore from the above figure, $\cos \theta = \frac{p_z}{|\vec{p}|} = \frac{p_z}{E}$,

$$y = \frac{1}{2} \ln \left(\frac{1 + \cos \theta}{1 - \cos \theta} \right) = \frac{1}{2} \ln \left(\frac{2 \cos^2 \theta}{2 \sin^2 \theta} \right) = \frac{1}{2} \ln \left(\cot^2 \frac{\theta}{2} \right) \quad (7.49)$$

Therefore, we define,

$$\eta \equiv \ln \left(\cot \frac{\theta}{2} \right) \quad (7.50)$$

η is a geometric quantity i.e. it is a function θ . Rapidity and pseudorapidity match in the massless limit. [\[32\]](#)

7.3.3 Observables

Collider observables depend on the momentum and energy of the produced particles. Ideally, we aim to measure the 4-momentum of each particle in an event, but this is often impractical. As a first approximation, we can measure the energy of stable

particles within detector timescales, using deposits in calorimeters, along with their directions (η, ϕ) . We can reconstruct the three momenta of the particles using this information. [30] [20]

1. *Invariant Mass M*

The invariant mass of two particles say i and j is defined as follows:

$$m_{ij}^2 = \sqrt{(E_i + E_j)^2 - (\vec{p}_i + \vec{p}_j)^2} \quad (7.51)$$

The Higgs boson at the LHC was observed as a peak in the Invariant mass of diphoton $(\gamma\gamma)$

2. *Missing Transverse Energy or MET (E_T)*

The transverse momentum of undetected particles, often referred to as missing transverse momentum (MET), can be inferred by examining the momentum imbalance in the transverse direction caused by visible particles.

$$E_T = \sqrt{(\sum_{l,j,\gamma} p_x)^2 + (\sum_{l,j,\gamma} p_y)^2} \quad (7.52)$$

Where the sum includes momentum of all the visible particles like leptons (l), jets (j), and photons (γ).

3. *Missing Energy or ME (E)*

At lepton colliders, we can infer the energy carried away by undetected particles by utilizing the known center-of-mass energy \sqrt{s}

$$E = \sqrt{s} - \sum_{l,j,\gamma} (E_{visible}) \quad (7.53)$$

Where the sum includes the energy of all the visible particles like leptons (l), jets (j), and photons (γ).

4. *Missing Mass or MM (M)*

This variable is useful if the initial state of four momenta of the particles is known.

$$M^2 = (\sum_i (p_i) - \sum_{l,j,\gamma} (p))^2 \quad (7.54)$$

Where the last summation is over all visible final state particles. In the context of ILC, for the mono- γ process in the production of DM χ , $e^+e^- \rightarrow \chi\chi\gamma$,

$$m_{\text{miss}}^2 = s - 2\sqrt{s}E_\gamma \quad (7.55)$$

\cancel{E} and \cancel{M} are useful observables in the context of ILC, while at the LHC due to unknown $\sqrt{\hat{s}}$ only MET is useful.

7.3.4 Simulation framework

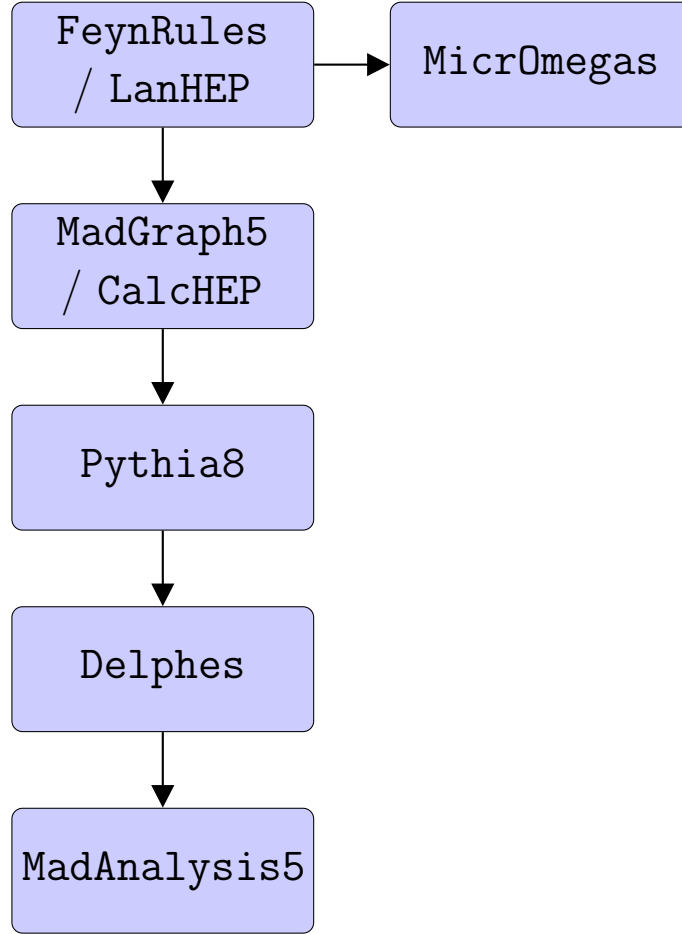


Fig. 7.2 Simulation Flowchart

The BSM model is first implemented in **FeynRules** [22] or **LanHEP** [23]. The model file is then passed to Monte Carlo event generators **MaGraph5** [25] or **CalcHEP** [34] for parton level calculation. **Pythia8** [26] handle parton showering and Hadronization. The detector level simulation is done by **Delphes** [31]. **MadAnalysis5** [35] is a framework used for analysis of event field generated by Monte Carlo event generators. **MicrOmegas** [24] is a package for the calculation of Dark Matter properties.

List of Figures

2.1	Rotation curves of spiral galaxies showing the flattening behavior at larger distances. [5] The image is taken from a paper by Rubin 1980 [6]	8
2.2	(a) Einstein ring/arcs due to <i>SDSSJ0146 – 0929</i> galaxy cluster as a result of Strong Lensing; Credits: NASA/Hubble Space Telescope [7]. (b) Bullet Cluster (1E0657-56) Credits: NASA/ESA [8]	9
2.3	The logarithmic plot illustrates the decoupling of a cold Dark Matter relic with a mass of $m_{\text{DM}} = 100 \text{ GeV}$ and $n = 0$. The black line represents the equilibrium distribution, while the other lines depict the actual abundance.	10
2.4	Here, the black dotted line shows yield at infinity which gives the correct relic density and corresponds to $\sigma_0 = 1.33 \times 10^{-9}$ for $m_{\text{DM}} = 100 \text{ GeV}$ and $n = 0$	12
2.5	Pictorial representation of Dark Matter searches. The image is taken from [3]	12
3.1	Pictorial representation of Bottom-Up and Top-Down approaches. The image is taken from [14]	16
3.2	Tree level process for β decay	17
3.3	Fermi's effective four fermion vertex for β decay [17]	17
4.1	DM-nucleon scattering via one loop coupling with leptons. The image is taken from paper	22
4.2	(a) Evolution of yield keeping $(m_{\text{DM}}, c) = (300 \text{ GeV}, 1)$ fixed and varying New physics scale, $\Lambda = (1.5, 2.3, 4) \text{ TeV}$. (b) Varying Wilson coefficient, $c = (0.7, 1.7, 3.5)$ while keeping $(m_{\text{DM}}, \Lambda) = (300 \text{ GeV}, 3 \text{ TeV})$ fixed	24
4.3	Two parameters, the new physics scale Λ and DM mass M_χ varied in the range of $1 - 10^4$ with all the operators combined $(c_{l1}, c_{l2}, c_{l3}, c_{l4}) = (1, 1, 1, 1)$	24

4.4	Initial State Radiation (ISR) with DM pair production. Here, the blob represents the effective DM-SM vertex. [20]	26
4.5	Variation of $\sigma_{e^+e^- \rightarrow \chi\bar{\chi}}$ as a function of \sqrt{s} (a), Λ (b), m_χ (c) and couplings, c_{l_i} (d) for Dirac DM (BP1) for three different choices of beam polarization.	27
4.6	a) Adding cross-section of all C_{l_i} individually and comparing it with all taken at once for unpolarized beam. (b) Individual C_{l_i} variation of cross-section with CM energy \sqrt{s}	27
4.7	(a) Adding cross-section of all C_i individually and comparing it with all taken at once for unpolarized beam. (b) Individual C_i variation of cross-section with $\text{Log}\Lambda$	28
4.8	(a) Adding cross-section of all C_i individually and comparing it with all taken at once for unpolarized beam. (b) Individual C_i variation of cross-section with $\text{Log}m_\chi$	28
4.9	s and t channel Feynman diagrams for the SM background process, $e^+e^- \rightarrow \nu_e\bar{\nu}_e$. Mono-photon events will arise from ISR [17]	29
4.10	a) Normalized mono- γ distribution for the BP1, BP2, and background as a function of missing transverse energy (MET) (b) Normalized mono- γ distribution for the BP1, BP2, and background as a function of missing energy (\cancel{E})	30
4.11	a) Normalized mono- γ distribution for the BP1, BP2, and background as a function of photon energy E_γ (b) Normalized mono- γ distribution for the BP1, BP2, and background as a function of missing mass (m_{miss})	30
5.1	Feynman diagram corresponding to Mono-X signal and DM pair production with effective vertex represented by blob. Here, V represents γ, Z, H [28]	34
5.2	Two peak behavior combinations. Individual Normalized \cancel{E} distributions for mono-Z and mono-H signals arising from operators: (a) \mathcal{O}_1^f and \mathcal{O}_3^s (b) \mathcal{O}_2^s and \mathcal{O}_1^s . Here, the masses of DM candidates are chosen to be 100 GeV (\mathcal{O}_2^s and \mathcal{O}_3^s) and 400 GeV (\mathcal{O}_1^s and \mathcal{O}_1^f). We choose $\Lambda = 1.2\text{TeV}$, $\sqrt{s} = 1\text{ TeV}$ with $(P_e^+, P_e^-) : (+30\%, +80\%)$	35
5.3	Two peak behavior combinations. Individual Normalized \cancel{E} distributions for the mono- γ signal arising from operators: (a) \mathcal{O}_3^s and \mathcal{O}_2^f (b) \mathcal{O}_3^f and \mathcal{O}_2^f . Here, the masses of DM candidates are chosen to be 100 GeV (\mathcal{O}_3^s and \mathcal{O}_3^f) and 200 GeV (\mathcal{O}_2^f). We choose $\Lambda = 1.2\text{TeV}$, $\sqrt{s} = 1\text{ TeV}$ with $(P_e^+, P_e^-) : (+30\%, +80\%)$	36

5.4	s and t channel Feynman diagrams for the SM background process, $e^+e^- \rightarrow \nu_e \bar{\nu}_e$. Mono-X events will arise from ISR [17]	36
5.5	Signal together with background $\nu\nu\gamma$. Normalized \cancel{E} distributions for the mono- γ signal arising from operates: (a) \mathcal{O}_3^s (100 GeV) and \mathcal{O}_2^f (200 GeV) (b) \mathcal{O}_3^f (100 GeV) and \mathcal{O}_2^f (200 GeV). We choose $\Lambda = 1.2TeV$, $\sqrt{s} = 1$ TeV with $(P_e^+, P_e^-) : (+30\%, +80\%)$	37
5.6	Signal together with background. Normalized \cancel{E} distributions from operates: (a) Mono-Z: \mathcal{O}_3^s (100 GeV) and \mathcal{O}_1^f (400 GeV) (b) Mono-H: \mathcal{O}_2^s (100 GeV) and \mathcal{O}_1^s (400 GeV). We choose $\Lambda = 1.2TeV$, $\sqrt{s} = 1$ TeV with $(P_e^+, P_e^-) : (+30\%, +80\%)$	37
5.7	$t \equiv \cancel{E}$ distribution with $y \equiv d\sigma/d\cancel{E}$ quantifying C3 and C4 parameters. The image is taken from paper [30]	38
5.8	(a) Cross-section variation with DM mass for operators giving the mono-Z signal. (b) Cross-section variation with DM mass for operators giving the mono- γ signal. For both the cases, $\sqrt{s} = 1$ TeV, $C_{DM} = 1$, $\Lambda = 1200$ GeV and Polarization: $(P_e^+, P_e^-) = (30\%, 80\%)$ is set.	40
5.9	(a) Variation of signal significance in \cancel{E} distribution for operators $(\mathcal{O}_3^s, \mathcal{O}_2^f)$ for two sets of DM mass. (b) Variation of signal significance in \cancel{E} distribution for operators $(\mathcal{O}_3^f, \mathcal{O}_2^f)$ for two sets of DM mass. For both the cases, $\sqrt{s} = 1$ TeV, $(C_{DM1}, C_{DM2}) = (1.5, 1)$, $\Lambda = 1200$ GeV and Polarization: $(P_e^+, P_e^-) = (30\%, 80\%)$ is set.	40
5.10	(a) Variation of signal significance in \cancel{E} distribution for operators $(\mathcal{O}_3^s, \mathcal{O}_1^f)$: Mono-Z $(C_{DM1}, C_{DM2}) = (2, 1)$. (b) Variation of signal significance in \cancel{E} distribution for operators $(\mathcal{O}_2^s, \mathcal{O}_1^s)$: Mono-H $(C_{DM1}, C_{DM2}) = (1, 1)$. For both the cases, $\sqrt{s} = 1$ TeV, $\Lambda = 1200$ GeV and Polarization: $(P_e^+, P_e^-) = (30\%, 80\%)$ is set	40
6.1	Relic density allowed parameter space in $m_{dm1} - C_{dm1}$ plane. Different colors indicate the percentage of relic density. New Physics scale, $\Lambda = 1200$ GeV is set.	43
6.2	Relic density allowed parameter space in $m_{dm2} - C_{dm2}$ plane. Different colors indicate the percentage of relic density. New Physics scale, $\Lambda = 1200$ GeV is set.	43
6.3	Left: $(\mathcal{O}_1^f, \mathcal{O}_3^s) = (10\%, 90\%)$ Middle: $(\mathcal{O}_1^f, \mathcal{O}_3^s) = (50\%, 50\%)$ Right: $(\mathcal{O}_1^f, \mathcal{O}_3^s) = (90\%, 10\%)$; contribution $C_{DM}M_{DM}$ plane	44
7.1	Polar angle: θ ; Pseudorapidity η and Lorentz invariant quantity, Azimuthal angle: ϕ	57

7.2	Simulation Flowchart	60
-----	--------------------------------	----

List of Tables

1.1	The Standard Model fermions characterized by their quantum numbers, which include their electric charge (Q), measured in units of the elementary charge (e), the third component of weak isospin (I^3), hypercharge (Y), and color charge (r, g, b, corresponding to red, green, and blue) [2]	3
1.2	An overview of the bosons in the SM.	3
4.1	Here, χ is a DM fermion, $B^{\mu\nu 1}$ refers to $U(1)_Y$ gauge field strength tensor, H stands for the SM Higgs doublet, and $\sigma_{\mu\nu}^2$ refers to the Pauli spin matrices, describing the spin of particles.[20]	21
4.2	Here, l stands for either left handed doublet(LH) or right handed (RH) singlet SM lepton. q stands for LH doublet or RH singlet SM quarks of all flavours and χ denotes the DM fermion.[20]	21
4.3	Benchmark Points for Dirac DM scenario. Here, Model refers to choices of Wilson coefficients.	25
5.1	φ is a scalar DM and χ is a fermionic DM, $L(l_R)$ is the left (right)-handed SM lepton doublet (singlet), $B_{\mu\nu}$ and $W_{\mu\nu}$ are the electroweak field strength tensors, Φ is the SM Higgs doublet, D_μ is the gauge-covariant derivative, and Λ is the new physics (NP) scale of the EFT operators.	33
5.2	Benchmark points in Mono-X	39

References

- [1] Matthew D. Schwartz. *Quantum Field Theory and the Standard Model*. Cambridge University Press, 3 2014.
- [2] Moritz Habermehl. *Dark Matter at the International Linear Collider*. PhD thesis, Hamburg U., Hamburg, 2018.
- [3] Mathias Pierre. Dark matter phenomenology: from simplified wimp models to refined alternative solutions. *arXiv preprint arXiv:1901.05822*, 2019.
- [4] Gianfranco Bertone and Dan Hooper. History of dark matter. *Reviews of Modern Physics*, 90(4):045002, 2018.
- [5] Mariangela Lisanti. Lectures on dark matter physics. In *New Frontiers in Fields and Strings: TASI 2015 Proceedings of the 2015 Theoretical Advanced Study Institute in Elementary Particle Physics*, pages 399–446. World Scientific, 2017.
- [6] Vera C Rubin, W Kent Ford Jr, and Norbert Thonnard. Rotational properties of 21 sc galaxies with a large range of luminosities and radii, from ngc 4605/ $r=4\text{kpc}$ /to ugc 2885/ $r=122\text{ kpc}$. *Astrophysical Journal, Part 1, vol. 238, June 1, 1980, p. 471-487.*, 238:471–487, 1980.
- [7] NASA. Hubble finds an einstein ring, 2015.
- [8] The bullet cluster, 2007.
- [9] Edward W Kolb and Michael S Turner. The early universe. *Nature*, 294(5841):521–526, 1981.
- [10] Stefano Profumo. *An introduction to particle dark matter*. World Scientific Publishing Company, 2017.
- [11] Flip Tanedo. Defense against the dark arts. *Notes on dark matter and particle physics*, 2011.

- [12] Peter AR Ade, Nabila Aghanim, M Arnaud, Mark Ashdown, J Aumont, Carlo Baccigalupi, AJ Banday, RB Barreiro, JG Bartlett, N Bartolo, et al. Planck 2015 results-xiii. cosmological parameters. *Astronomy & Astrophysics*, 594:A13, 2016.
- [13] Aneesh V. Manohar. Introduction to Effective Field Theories. 4 2018.
- [14] Rafael Aoude. *Effective Field Theory Phenomenology and Scattering Amplitudes*. PhD thesis, Mainz U., 2020.
- [15] R P Feynman and M Gell-Mann. Theory of the fermi interaction. *Physical Review (U.S.) Superseded in part by Phys. Rev. A, Phys. Rev. B: Solid State, Phys. Rev. C, and Phys. Rev. D*.
- [16] Coenraad B. Marinissen, Rudi Rahn, and Wouter J. Waalewijn. ..., 83106786, 114382724, 1509048322, 2343463290, 27410087742, ... efficient Hilbert series for effective theories. *Phys. Lett. B*, 808:135632, 2020.
- [17] Joshua P Ellis. Tikz-feynman: Feynman diagrams with tikz. *Computer Physics Communications*, 210:103–123, 2017.
- [18] Subhaditya Bhattacharya and Jose Wudka. Effective theories with dark matter applications. *Int. J. Mod. Phys. D*, 30(13):2130004, 2021.
- [19] Basabendu Barman, Subhaditya Bhattacharya, and Bohdan Grzadkowski. Feebly coupled vector boson dark matter in effective theory. *JHEP*, 12:162, 2020.
- [20] Barman Basabendu, Bhattacharya Subhaditya, Girmohanta Sudhakantha, and Jahedi Sahabub. Effective leptophilic wimps at the e+ e- collider. *Journal of High Energy Physics*, 2022(4), 2022.
- [21] Philip Bambade, Tim Barklow, Ties Behnke, Mikael Berggren, James Brau, Philip Burrows, Dmitri Denisov, Angeles Faus-Golfe, Brian Foster, Keisuke Fujii, et al. The international linear collider: a global project. *arXiv preprint arXiv:1903.01629*, 2019.
- [22] Adam Alloul, Neil D Christensen, Céline Degrande, Claude Duhr, and Benjamin Fuks. Feynrules 2.0—a complete toolbox for tree-level phenomenology. *Computer Physics Communications*, 185(8):2250–2300, 2014.
- [23] AV Semenov. Lanhep—a package for the automatic generation of feynman rules in field theory. version 3.0. *Computer Physics Communications*, 180(3):431–454, 2009.

- [24] G Alguero, D Barducci, G Bélanger, F Boudjema, J Da Silva, A Goudelis, S Kraml, U Laa, A Mjallal, A Pukhov, et al. The micromegas user’s manual, version 5.3. 34. 2022.
- [25] Johan Alwall, R Frederix, S Frixione, V Hirschi, Fabio Maltoni, Olivier Mattelaer, H-S Shao, T Stelzer, P Torrielli, and M Zaro. The automated computation of tree-level and next-to-leading order differential cross sections, and their matching to parton shower simulations. *Journal of High Energy Physics*, 2014(7):1–157, 2014.
- [26] Torbjörn Sjöstrand, Stefan Ask, Jesper R. Christiansen, Richard Corke, Nishita Desai, Philip Ilten, Stephen Mrenna, Stefan Prestel, Christine O. Rasmussen, and Peter Z. Skands. An introduction to PYTHIA 8.2. *Comput. Phys. Commun.*, 191:159–177, 2015.
- [27] J. de Favereau, C. Delaere, P. Demin, A. Giammanco, V. Lemaître, A. Mertens, and M. Selvaggi. DELPHES 3, A modular framework for fast simulation of a generic collider experiment. *JHEP*, 02:057, 2014.
- [28] Subhaditya Bhattacharya, Purusottam Ghosh, Jayita Lahiri, and Biswarup Mukhopadhyaya. Mono-x signal and two component dark matter: new distinction criteria. *arXiv preprint arXiv:2211.10749*, 2022.
- [29] Subhadittya Bhattacharya, Aleksandra Drozd, Bohdan Grzadkowski, and Jose Wudka. Two-component dark matter. *Journal of High Energy Physics*, 2013(10):1–31, 2013.
- [30] Subhaditya Bhattacharya, Purusottam Ghosh, Jayita Lahiri, and Biswarup Mukhopadhyaya. Distinguishing two dark matter component particles at e+e- colliders. *Journal of High Energy Physics*, 2022(12):1–52, 2022.
- [31] Michele Selvaggi. Delphes 3: A modular framework for fast-simulation of generic collider experiments. In *Journal of Physics: Conference Series*, volume 523, page 012033. IOP Publishing, 2014.
- [32] Matthew D Schwartz. Tasi lectures on collider physics. In *Anticipating the Next Discoveries in Particle Physics: TASI 2016 Proceedings of 2016 Theoretical Advanced Study Institute in Elementary Particle Physics*, pages 65–100. World Scientific, 2018.
- [33] Tao Han. Collider phenomenology: Basic knowledge and techniques. In *Theoretical Advanced Study Institute in Elementary Particle Physics: Physics in $D \geq 4$* , pages 407–454, 8 2005.

- [34] Alexander Belyaev, Neil D. Christensen, and Alexander Pukhov. CalcHEP 3.4 for collider physics within and beyond the Standard Model. *Comput. Phys. Commun.*, 184:1729–1769, 2013.
- [35] Eric Conte, Benjamin Fuks, and Guillaume Serret. Madanalysis 5, a user-friendly framework for collider phenomenology. *Computer Physics Communications*, 184(1):222–256, 2013.